Chaos, Solitons and Fractals 81 (2015) 246–270

Contents lists available at ScienceDirect

Chaos, Solitons and Fractals

Nonlinear Science, and Nonequilibrium and Complex Phenomena

journal homepage: www.elsevier.com/locate/chaos

Quasi-periodic fractal patterns in geomagnetic reversals, geological activity, and astronomical events

Stephen J. Puetz [a,*], Glenn Borchardt [b]

[a] Progressive Science Institute, Honolulu, HI 96815, USA
[b] Soil Tectonics, Box 5335, Berkeley, CA 94705, USA

ARTICLE INFO

Article history:
Received 27 May 2015
Accepted 25 September 2015

Keywords:
Harmonics
Fractals, period-tripling
Geomagnetic reversal
Spectral analysis
Cycles

ABSTRACT

The cause of geomagnetic reversals remains a geological mystery. With the availability of improved paleomagnetic databases in the past three years, a reexamination of possible periodicity in the geomagnetic reversal rate seems warranted. Previous reports of cyclicity in the reversal rate, along with the recent discovery of harmonic cycles in a variety of natural events, sparked our interest in reevaluating possible patterns in the reversal rate. Here, we focus on geomagnetic periodicity, but also analyze paleointensity, zircon formation, star formation, quasar formation, supernova, and gamma ray burst records to determine if patterns that occur in other types of data have similar periodicity. If so, then the degree of synchronization will indicate likely causal relationships with geomagnetic reversals. To achieve that goal, newly available time-series records from these disciplines were tested for cyclicity by using spectral analysis and time-lagged cross-correlation techniques. The results showed evidence of period-tripled cycles of 30.44, 91.33, 274, 822, and 2466 million years, corresponding to the periodicity from a new Universal Cycle model. Based on the results, a fractal model of the universe is hypothesized in which sub-electron fractal matter acts as a dynamic medium for large-scale waves that cause the cycles in astronomical and geological processes. According to this hypothesis, the medium of sub-electron fractal matter periodically compresses and decompresses according to the standard laws for mechanical waves. Consequently, the compressions contribute to high-pressure environments and vice versa for the decompressions, which are hypothesized to cause the instabilities that lead to episodic astronomical and geological events.

1. Introduction

The occurrence of geomagnetic reversals remains one of the most puzzling aspects of geological processes. Fifty years ago, Hospers [38] introduced the Geocentric Axial Dipole (GAD) Hypothesis, which gives researchers a method for estimating the location of the rotational axis of the geographic pole. The GAD Hypothesis assumes that the magnetic pole randomly gyrates around the axial pole [12]. Based on this assumption, researchers sample rocks and sediments to determine remanent magnetism, often spanning a period of 10–100 thousand years (kyr). The goal is to find a site-mean Virtual Geomagnetic Pole that should coincide with the rotational axis of the geographic pole [12,60].

Soon after the GAD Hypothesis gained support, other researchers claimed that geomagnetic reversals contributed to mass extinctions [32,102]. Subsequently, Phillips and Cox [76] used a dataset of polarity reversals for the interval from 46 to 0 Ma and found no evidence for cycles in polarity. Although not directly relevant to the GAD hypothesis, this

* Corresponding author. Tel.: +1 808 840 0933.
E-mail addresses: puetz.steve@gmail.com (S.J. Puetz), gborchardt@gmail.com (G. Borchardt).

http://dx.doi.org/10.1016/j.chaos.2015.09.029

further supported the belief in random oscillations in the location of the geomagnetic pole. However, the limited extent of the data used by Phillips and Cox [76], which covered only 46 million years (myr), casts some doubt on the reliability of their conclusion.

Soon afterward, Raup and Sepkoski [83] found an approximately 30-myr cycle in mass extinctions in the marine fossil record. They suggested that an extraterrestrial factor might cause the cycles. Then Raup [84] used a 165-myr time-series that indicated geomagnetic reversals occur in cycles nearly identical to the 30-myr cycle in mass extinctions. Negi and Tiwari [63] were the first to study geomagnetic reversal periodicity over an extensive interval (570-myr)—finding cycles of 285, 114, 71–64, 47 and 34–32 myr. About the same time, Mazaud et al. [57] found a 15-myr cycle in geomagnetic reversals by using data spanning the last 100-myr. However, Lutz [55] soon countered that the magnetic reversal record was not periodic.

As improved geomagnetic records became available, and extended further into the past, more meaningful studies proliferated. Stothers [95] used data spanning the past 165-myr that contained 296 reversals and found harmonic cycles of approximately 15-myr and 30-myr—thus confirming the earlier discovery of Mazaud et al. [57]. Stothers also noted that the periodicity seemed to coincide with cycles in tectonic activity and asteroid impacts. Then Loper et al. [53] proposed a model of cyclicity in Earth's mantle and core to explain the correlated periodicity in geomagnetic reversals, volcanism, tectonic activity, climate, sea level variation, impact cratering, and mass extinctions.

During this period, researchers developed a variety of theories involving various sequences and/or combinations of correlated periodic events, such as: passage of the Solar System through the galactic plane, asteroid impacts, geomagnetic reversals, volcanism, geo-marine processes, sea-level variation, and mass extinctions [64,65,81,82,98,99].

Tiwari and Rao [97] developed the most inclusive of these theories, which aimed to explain the correlated variations and periodicity of ~30-myr in global CO_2, mantle convection, geomagnetic reversals, volcanism, tectonic activity, asteroid bombardments, and mass extinctions. Accordingly, they suggested an external factor, as did Raup and Sepkoski [83], as the cause of the quasi-periodic mass extinctions. Tiwari and Rao [97] suggested that the external forcing mechanism came from the periodic bombardment of asteroids, which contributed to a chain of events—first altering the geotectonic and geomagnetic states, and then causing volcanic, climatic, and reversal events that ended with mass extinctions.

In addition to cycles in the reversal rate, other researchers suspected a cycle in superchrons, which are intervals lasting millions of years without a reversal. Johnson et al. [42] indicated a ~200-myr cycle in superchrons, possibly caused by movements of the Solar System through the spiral arms of the galaxy. Then Jacobs [40] discussed what he thought to be the internal and external mechanisms for the formation of superchrons. These included the role of the inner core, true polar wander, Earth's orbital variations, and tides. Later, Wendler [108] proposed that the superchron cycle was ~180-myr, and also suggested that geomagnetic field periodicity resulted from external forcing. More recently, Biggin et al. [9] indicated a 180–190-myr cycle in superchrons, but hypothesized a link between long-term geomagnetic variations and whole-mantle convection processes.

Of course, these estimates of superchron periodicity were based on only three cycles, thus making their significance less than conclusive. Nonetheless, these studies were based on obvious variation in reversal occurrence—enough so that the reversal rate cannot be considered uniform. The observations from Johnson et al. [42], Jacobs [40], Wendler [108], and Biggin et al. [9] contain a common theme of correlated periodicity among events from a variety of disciplines—even though each explains the superchron variation with a different cause. Butler [12] noted that all plausible theories of geomagnetism involve generating the field from within the fluid outer core of the Earth by a magneto–hydro-dynamic process. To this day, most researchers continue to focus on internal geo-dynamics to explain geomagnetic variation and/or periodicity. Internal mechanics contribute significantly to geomagnetic variation, but some suspect that external mechanisms also contribute to the variation.

2. Fractals

This work focuses on fractals, and analyzes how they might cause the periodicity in astronomical and geological activity. Fractals occur throughout nature, and are often described as being scale-invariant or self-similar [25,56,101]. In mathematics, *scale-invariance* refers to features that remain *exactly the same* even after scales such as length or time are multiplied by a common factor. This idealized mathematical state is convenient for developing equations. However, in physics and geology, observations never match the idealized perfection of scale-invariance. In the natural sciences, the term *self-similar* is used to describe features that remain *approximately the same* even after the scales are multiplied by a common factor. Scale-invariance (mathematical idealization) and self-similarity (natural occurrence) are typical properties associated with fractals and are sometimes used interchangeably.

Nearly 50 years ago, Mandelbrot [56] introduced the idea of fractals occurring in nature when he asked a seemingly simple question: How long is the coast of Britain? He then explained that geographical curves are so complicated that details about their lengths are often undefinable. He then showed that coastlines are statistically self-similar—with each portion of the coast considered as a reduced-scale image of the whole.

Later, Feigenbaum [25] introduced a nonlinear universal scale-invariant model for physical processes occurring in period-doubled sequences—thus mathematically describing fractals in terms of cycles. After applying these concepts to Earth sciences, Turcotte [101] stated that geological formations were fractal. Later still, McCaffrey and Petford [58] focused on granitic intrusions and found they were fractal.

In fact, the fractal patterns extend well beyond the confines of Earth. At an astronomical scale, Pietronero [77] demonstrated the occurrence of a single fractal (self-similar) structure that extends from the galaxy-scale up to the limits of astronomical observations. More recently, Joyce et al. [43] used data from the Sloan Digital Sky Survey to show that the distribution of galaxies is well described by a fractal dimension of $D \approx 2$ up to a scale of at least 20 Mpc/h (roughly a distance of 100 million light years).

Along these lines, Puetz et al. [80] found highly significant cycles of 822-myr and 274-myr in the formation of stars in the regions surrounding the Solar System. Interestingly, Isley and Abbott [39] studied a time-series of ultramafic and mafic rocks with the major peaks in the time series inferred to represent mantle plume events. They found strong periodicity of 819-myr and 273-myr in rock formation, and concluded that the 819-myr cycle is significantly longer than any periodic, tectonically driven process. Of course, these geological cycles are nearly identical to the ~822-myr and ~274-myr astronomical cycles in star formation.

Although fractal cosmology remains a minority view for explaining the occurrence of events in the universe, we prefer a fractal model because it fits well with established observations—as well as explaining some new and unexpected observations such as dark-flow [45,46] and the detection of a dipole in the handedness of spiral galaxies [52].

NASA astrophysicists [45,46] recently found a strong and coherent bulk flow of galaxy clusters to a distance of at least 800 Mpc, which was the limit of their data. They noted that the theoretical framework defined by the Lambda cold dark matter (ΛCDM) cosmological model cannot easily explain this directional flow of galaxy clusters—thus, indicating the need for new ideas about large-scale motions. They interpreted the finding as evidence of a uniform gravitational movement of the galaxy clusters related to an immense mass that lies beyond the observable regions of the universe.

Shortly afterward, Longo [52] found another violation of the cosmological principle from a statistically significant excess of left-handed spiral galaxies toward the North Galactic Pole and an excess of right-handed spiral galaxies in the opposite direction. Longo [52] interpreted this finding as evidence that the galaxies in the observable regions of the universe are rotating around a preferred axis, with a net angular momentum. Since angular momentum is conserved, this implies that these regions of the universe have been spinning in a vortex for billions of years. Importantly, the finding indicates that all matter within the observed regions of the universe is spinning in a vortex similar to most astronomical objects found within and beyond the Solar System. Very likely, this indicates a still larger collection of matter in a hierarchical sequence of fractals.

Our preference for using a fractal model of the universe for explaining cyclical formations does not imply that the existing set of standard physical equations must be tossed out. Quite the contrary, the equations themselves are fairly reliable and only require the addition of a simple ± factor for measurement errors and anomalies. The only major revisions to existing theories would be philosophical. That is, the vast collection of new and old evidence indicates employing a philosophy of an infinite and fractal universe instead of the currently preferred philosophy of a finite universe consisting of significant empty-space. In an infinitely fractal universe, perfectly empty-space is an unachievable ideal. In the fractal model espoused here, we assume that all matter consists of smaller types of matter—while also integrating with similar types of matter to form larger objects. Based on this model, the motions associated with harmonically-related waves are considered as integrals of longer-period cycles—as well as being multiples of shorter-period cycles. However, no cycle (at any scale) is more fundamental than another cycle (at another scale).

3. Universal Cycle model

The rich record of periodicity in natural events, including the frequency of geomagnetic reversals, indicates the need for an encompassing model to describe all of the correlated happenings. Following Feigenbaum [25], we devised a "universal" nonlinear scale-invariant fractal model for physical processes–developed in terms of time (periodicity) rather than distance (length or wavelength). However, unlike the period-doubling model of Feigenbaum [25], the model here requires a primary period-tripling component—along with period-halving sub-components.

The primary cyclic components of the Universal Cycle model develop in a geometric progression with a common ratio of 3 [79,80]. The cycles are considered "universal" because the same cyclic progressions occur in astronomical, geological, and genetic contexts ranging from decades to billions of years. The data indicate that the components of the model, the Universal Wave Series (UWS) cycles, originate from a common non-linear forcing mechanism, but the phases of the waves apparently transmit linearly (with possible delay) to cause the observed natural cycles. The Universal Cycle model, consisting of an unlimited number of individual UWS cycles, has hypothetical periods of

$$P_{k,n} = \left(\frac{3^k}{2^n}\right) P_{0,0} \tag{1}$$

where k is a positive or negative integer corresponding to a cycle in the primary period-tripling sequence, n is one of eight period-halving harmonics where $n \in \{0, 1, 2, 3, 4, 5, 6, 7\}$, and $P_{0,0}$ is a base cycle with a period of 2.82894367327307 solar years. Eq. (1) gives the periods of the UWS cycles being tested with spectral analysis. The dominant period-halving UWS cycles ($n = 0, 1, 2, 3$) are found more often in the periodograms and normally show higher confidence levels than the secondary period-halving UWS cycles ($n = 4, 5, 6, 7$).

The composite stochastic Universal Cycle model consists of a superposition of cosine waves, with periods of $P_{k,n}$ from Eq. (1), corrupted by Gaussian white noise, and are of the form

$$y_i = \sum_{k=k_1}^{K} \sum_{n=n_1}^{N} A_{k,n} \cos\left(\frac{2\pi\,(t_i + \phi)}{P_{k,n}}\right) + \sigma Z_i \tag{2}$$

where $i = 1, 2, 3,\ldots$, I are the records in a time-series, K is a set of consecutive integers, N is the integer set {0, 1, 2, 3, 4, 5, 6, 7}, $A_{k,n}$ are non-negative amplitude factors, t_i are negative numbers for times in the past and positive for times in the future, ϕ is a phase adjustment so that all UWS cycles peak synchronously at time ϕ. The Universal Cycle model is not intended as a model for all cycles found in nature. Instead, it describes an important fractal subset of natural cycles. Accordingly, Z_i are independent random variables with standard normal distributions, with $\sigma > 0$, representing noise and other non-UWS cyclical variation in the signal. The simplest model for the noise is additive Gaussian white noise, but more sophisticated models can be used.

Previously, we developed individual models for the most apparent UWS cycles—those for the consecutive integers $k \in$

{4, 5, 6,..., 19} and $n \in \{1, 2\}$ [80]. These individual models give perfect UWS cycles (without noise), are special cases of Eq. (2), and are of the form

$$y_i = \sum_{k\in K}\sum_{n\in N} A_{k,n} \cos\left(\frac{2\pi\,(t_i + \phi_0)}{P_{k,n}}\right) \quad (3)$$

where t_i are time-series ages (negative values for times in the past), and ϕ_0 is 2,722,762,372 years. Only the first four digits of ϕ_0 are precise at the myr-scale. The 10-digits allow calculating theoretical oscillations for all UWS cycles from 1 year to 1 billion years (gyr) with a single equation and with a single value for ϕ_0. Thus, setting ϕ_0 to 2723-myr would give sufficient precision when using the myr-timescale, and the first 7 digits of ϕ_0 would give sufficient precision for calculating phases for all kyr-cycles, but the full 10-digits of ϕ_0 must be used when calculating phases for cycles less than 1-kyr. Importantly, the likelihood of the model aligning with any set of natural records decreases with older ages—with any individual model possibly becoming asynchronous with a time-series after 50 oscillations beyond the present. The misalignment could result from errors in either the model, the timescales, or the ages of the records. The amplitude factors, $A_{k,n}$, remain unknown and should be set to 1 until estimates become available.

We must re-emphasize that the Universal Cycle model stipulates that every peak for a low-frequency UWS cycle aligns with a theoretical peak for every higher frequency UWS cycle. This requires a single value for ϕ_0 with many digits (2,722,762,372 years) so the equation aligns phases of all cycles with periods ranging from 1-yr to greater than 1-gyr.

4. Previously observed harmonics

Previously, others have noticed patterns similar to the harmonics described by the Universal Cycle model. The harmonics were found in geological, climatic, and solar records with periods ranging from 10.74-yr to 182.7-myr. For example, Belozerov and Ivanov [4] found that the sedimentary cover of the West Siberian plate has a periodic structure with repeated transgression-regression cycles and repeated local uplift cycles. They classified the major harmonics for three scales: (a) deposition cycles with periods of ~180-myr, (b) transgressions and regressions with periods of ~90-myr, and (c) stages of basin subsidence and uplift with periods of ~45-myr. Belozerov and Ivanov [4] rounded the cycles to integers ending in 0 and 5 (a technique often used by others). Even with the rounding, the harmonics closely corresponded to the 182.7-myr $P_{17,1}$, 91.33-myr $P_{17,2}$, and 45.67-myr $P_{17,3}$ cycles.

As already mentioned, Stothers [95] found harmonic cycles of 30 and 15-myr in geomagnetic reversals, which closely correspond to the 30.44-myr $P_{16,2}$ and 15.22-myr $P_{16,3}$ cycles.

In the kyr timescale, Lourens et al. [54] found climatic cycles of approximately 28, 41, 82, and 123-kyr in $\delta^{18}O$ records from the late Pliocene to the Pleistocene. They argued that the 28-kyr cycle reflects the sum frequency between the primary 41-kyr obliquity cycle and its multiples of 82-kyr and 123 kyr. We take a similar approach by also viewing the cycles as harmonic, but as the UWS sequence of 27.84-kyr $P_{9,1}$, 41.76-kyr $P_{10,2}$, 83.52-kyr $P_{10,1}$, and 125.3-kyr $P_{11,2}$ cycles.

Similarly, Pelletier [71] suggested a coherence resonance model for the harmonics associated with the 29 and 41-kyr cycles found in the Late Pleistocene climatic record. These also correspond reasonably well to the 27.84-kyr $P_{9,1}$ and 41.76-kyr $P_{10,2}$ cycles that we found.

Further down the timescale, Alvarez-Solas et al. [3] described climatic cycle harmonics with a model developed from records of Dansgaard–Oeschger cycles [21] and Heinrich cycles [34]. The harmonics from the model were multiples of the 1.5-kyr Dansgaard–Oeschger cycle with periods of 3.0, 4.5, 6.0, 7.5, and 9.0-kyr—roughly corresponding to the 1.547-kyr $P_{7,2}$, 3.093-kyr $P_{7,1}$, 4.640-kyr $P_{8,2}$, 6.187-kyr $P_{7,0}$, 7.830-kyr $P_{11,6}$, and 9.280-kyr $P_{8,1}$ UWS cycles.

In the sub-kyr timescale, Scafetta and Willson [86] found harmonic cycles in Hungarian auroral records that extend back to the year 1523. They found four major harmonics of 42.85, 57.13, 85.70, and 171.4-yr. The equivalent UWS cycles have nearly identical periods of 42.97-yr $P_{5,4}$, 57.29-yr $P_{4,2}$, 85.93-yr $P_{5,3}$, and 171.9-yr $P_{5,2}$—differing by only 0.28% from the harmonics they identified. The well-known harmonic Hale and Schwabe sunspot cycles also fit into this pattern, with the periods of the solar cycles corresponding with the 10.74-yr $P_{5,6}$ and 21.48-yr $P_{5,5}$ UWS cycles.

These previous harmonic discoveries have relevance for four reasons. First, the discoveries establish that other researchers have already found some of the patterns discussed here. Puetz et al. [80] built upon these findings by demonstrating that the cycles belong to a single harmonic set—the UWS cycles. Second, these earlier discoveries already showed that the $P_{k,1}$ and $P_{k,2}$ harmonics are the most common UWS cycles. Third, these discoveries show the multidisciplinary context of the harmonics. And fourth, this introduction to harmonics and periodic fractals sets the stage for an analysis of a particular set of period-tripled cycles—the sequence of 30.44-myr $P_{16,2}$, 91.33-myr $P_{17,2}$, 274-myr $P_{18,2}$, 822-myr $P_{19,2}$, and 2466-myr $P_{20,2}$ cycles.

5. Data

To perform this study, we used newly available data to demonstrate that astronomical factors contribute significantly to geological and geomagnetic variation. The investigation focused on four types of data with temporal resolution sufficient for analyzing cycles in the 20-myr to 2-gyr range. Five sets of geomagnetic reversal records were available. Data from Gradstein et al. [28] contained 939 reversals for the interval from 541 to 0 million years ago (Ma). Data from Pechersky [69] contained 624 reversals from 1691 to 0 Ma. An updated dataset from Pechersky et al. [70] contained 641 reversals, but with the samples restricted to the interval from 531 to 0 Ma. Version 4.6 of the Global Paleomagnetic Database [78] contains bipolar remanence records for the interval from 3452 to 0 Ma. Likewise, the Precambrian database PALEOMAGIA [103] contains records of bipolar remanence, with the records limited to the interval from 3482 to 540 Ma.

Others have noted that changes in the direction of bipolar remanence serve as legitimate proxies of ancient geomagnetic reversals [15,104,105]. We employ the same assumption. Rather than strictly defining polarity as either normal or reversed, Veikkolainen et al. [104] suggest using a time-averaged polarity state because of the increased

uncertainties associated with Precambrian measurements. The time-averaged polarity values range from 0% (all normal) to 100% (all reversed). Accordingly, we use that approach for the two paleomagnetic databases [78,103] in this study, and used time-averaged polarity values as proxies for geomagnetic reversals.

Gradstein et al. [28] noted the occasional difficulty in deciding whether an anomaly with a time-span of less than 30-kyr (a cryptochron) is a very short-lived polarity reversal or a geomagnetic excursion. Likewise, decisions about classifying a potential polarity chron as a subchron, and vice versa, are sometimes subjective. Nonetheless, when studying the periodicity of the reversal rate, the inclusion or omission of individual cryptochrons is not necessarily critical. For any type of natural phenomenon, a time-series is simply a sample of the true population. Whether the dataset has 500 samples or 1000 samples is somewhat irrelevant. The most important factor is that the datasets contain ages that are representative of the true population of reversals—which we assume to be true for the datasets in this work. If this assumption is false, then the spectral analysis results should identify any problematic datasets.

We used 4023 records from the latest version of the IAGA Paleointensity (PINT) Database, PINT 2014, to assess the periodicity of paleointensity. The IAGA PINT Database has undergone several upgrades over the past decade, including PINT 2003 [75], PINT 2006 [96], PINT 2009 [7], PINT 2010 [8], and PINT 2014 [10].

Periodicity in volcanic activity was determined from the ages of 197,519 zircons from Voice et al. [106] and 10,488 zircons from Condie [17].

Our study of cyclicity in star formation began with 11,799 solar-region stars from the Geneva–Copenhagen Survey with ages computed after implementing Hipparcos parallax revisions [37]—with the stars for this work restricted to those with age-errors either less than 2-gyr or less than 25% of the estimated ages of the stars. Casagrande et al. [13] used the same solar-region stars as Holmberg et al. [37], but applied a Padova Age Model to estimate the ages. Bergemann et al. [5] also assigned ages to solar-region stars by using the 143 samples from the Gaia-ESO Survey.

Next, we combined the records for ages of stars in globular clusters from regions far beyond the solar-region and into surrounding galaxies. This data allowed us to determine if the periodicity in solar-region star formation differed from the periodicity of star formation in surrounding galaxies. The globular cluster database included nine clusters from Canis Major [27], 80 clusters from the Large Magellanic Cloud (LMC) [31], 596 clusters from the Andromeda Galaxy (M31) [23,44] with duplicates removed, 671 clusters from the Pinwheel Galaxy (M33) [24], 74 clusters from the Milky Way Galaxy (MW) [27], and 11 clusters from Sagittarius [27]—giving a total of 1441 globular clusters in all. Hereafter, we refer to this collection of globular cluster records as the *GC-1441 Dataset*, which is available as supplementary information.

When massive stars die, the resulting explosion releases a brief but intense pulse of gamma rays—called a gamma ray burst (GRB). Because the gamma ray emissions are very short, it is not always possible to estimate redshift values for every GRB. However, we did obtain a reasonable sampling of the age-distribution of massive star deaths from 397 records of GRBs with redshift values [1,6,20,22,26,29,30,41,50,51,62,68,72–74,85,90,93]. Heretofore, we refer to these GRB records as the *GRB-397 Dataset*, which is available as supplementary information.

Similarly, supernova events indicate the deaths of medium-size stars. The Sloan Digital Sky Survey II (SDSS-II) database [47] contains redshift values for 4597 supernovae—thus allowing analysis of the age-distribution of medium-size stellar deaths. The analysis also includes 105,783 quasars with redshifts from the Sloan Digital Sky Survey, Data Release 7 (SDSS-DR7) [88], and 129,612 SDSS quasars and 15,043 Segue quasars with redshifts from the Sloan Digital Sky Survey, Data Release 10 (SDSS-DR10) [2]. To calculate gyr-age look-back times from the redshift values, we used the ΛCDM cosmological model parameter values $H_0 = 70.3$, $\Omega_\Lambda = 72.7\%$, and $\Omega_b + \Omega_c = 27.3\%$ [48].

This wide range of events was selected to test for periodicity in (a) astronomical formations (births) separately for the solar region, nearby galaxy region, and the farthest regions of the observable universe, and finally (b) astronomical deformations (deaths) in all regions of the observable universe.

6. Methods

Standard spectral analysis techniques [11,79,80,87,94] were used to assess periodicity. Then time-series plots were used to visualize the cycles, and the analyses concluded with time-lagged cross-correlation studies to determine the degree-of-fit between the data and the UWS model. Each test involved a relatively small range of frequencies, accomplished by applying an appropriate bandpass filter to the time-series before performing the analysis. Specifically, unwanted high-frequency cycles were removed by binning the data, and then unwanted low-frequency cycles were removed by applying a Gaussian filter to the binned data. After band-passing the data, spectral analysis was conducted with REDFIT software version 3.5 [89] by using Welch's method.

7. Interference patterns

A time-series plot is a vital analytical tool. In practice, analyses often start with a subjective inspection of a time series plot because it might show important features such as periodicity, trend, outliers, discontinuities, and localized anomalies that may contribute to an understanding of the underlying physics [14,100]. However, this type of subjective inspection for periodicity becomes complicated when multiple cycles occur with varying periodicity. The combination of waves from multiple cycles causes interference patterns that make each individual cycle either more visible (constructive interference) or less visible (destructive interference) in a time-series plot. Destructive interference is important because a cycle easily detected with a periodogram (an objective method for assessing cyclicity) might be difficult to see in a time-series plot. For the time-series plots in this work, interference patterns occur quite often between $P_{k,2}$-$P_{k-1,1}$ cycles and between $P_{k,2}$-$P_{k,3}$ cycles. The five panels in Fig. 1 illustrate how these interference patterns develop. Fig. 1a shows oscillations of the 274-myr $P_{18,2}$ cycle, Fig. 1b shows oscillations of the 182.7-myr $P_{17,1}$ cycle, and Fig. 1c

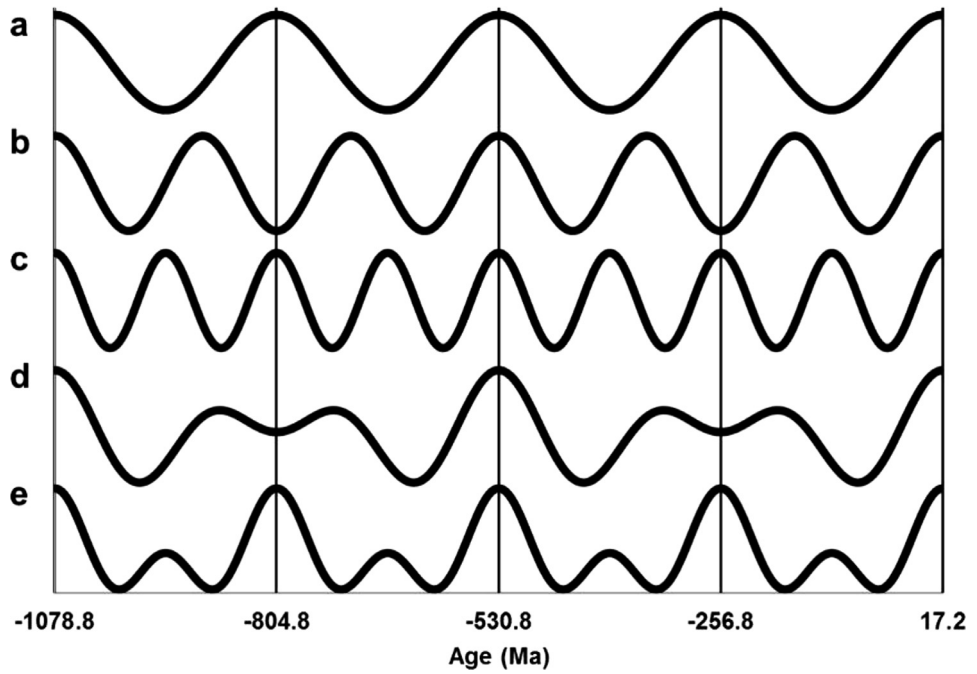

Fig. 1. Examples of wave interference patterns from the $P_{18,2}$, $P_{17,1}$, and $P_{18,3}$ idealized UWS cycles from Eq. (3) without noise. Panel a—274.0-myr $P_{18,2}$ cycle. Panel b—182.7-myr $P_{17,1}$ cycle. Panel c—137.0-myr $P_{18,3}$ cycle. Panel d—Interference pattern from combining the 274.0-myr and 182.7-myr cycles (panels a and b). Panel e—Interference pattern from combining the 274.0-myr and 137.0-myr cycles (panels a and c).

shows oscillations of the 137-myr $P_{18,3}$ cycle. Fig. 1d shows the interference pattern that develops after combining the waves from the 274-myr and 182.7-myr cycles.

In this particular case, the 182.7-myr cycle remains fairly obvious even though the amplitudes of the oscillations vary; however, the 274-myr cycle alternates between being very visible for one oscillation to being an indistinct dimpled-peak for the next oscillation. Fig. 1e shows the interference pattern that develops after combining the waves from the 274-myr and 137-myr cycles. In this instance, both cycles remain fairly obvious. The 274-myr cycle exhibits distinct peaks at the theoretical ages of 1078.8, 804.8, 530.8, 256.8 Ma, and 17.2 myr in the future, while the 137-myr cycle show large peaks at times corresponding to the 274-myr ages and smaller peaks between them.

Clearly, many different combinations of interference can develop. Fig. 1 only gives two examples of interference involving two cycles. The time-series plots become even more difficult to interpret when three or more cycles combine into complex interference patterns. For this reason, we used bandpass filters as a preliminary step in the analyses—to limit the number of cycles in each test, and accordingly to reduce the complexity of the test.

However, periodograms are the best objective means for assessing periodicity. While recognizing the value of time-series plots, they do have limitations. It is helpful to first view the periodograms to find the significance of the various cycles, and then view the time-series plots to assess how the cycles from the periodogram might combine into an interference pattern. When analyzed from this perspective, the time-series plots become meaningful. For this reason, the spectral analysis results precede the time-series plots for each separate analysis.

8. Results

The analysis involves the most obvious UWS cycle given by Eq. (3)—the $P_{k,2}$ sequence where $k = \{21,20,19,18,17,16\}$—progressing from the largest to the smallest UWS cycles. These cycles follow a theoretical tripling pattern of 7.398-gyr, 2.466-gyr, 822-myr, 274-myr, 91.33-myr, and 30.44-myr [80]. Other UWS cycles, especially those with periods equal to $P_{k,1}$ and $P_{k,3}$, also appear in the spectra quite often. In those situations, the correlation studies also include the $P_{k,1}$ and $P_{k,3}$ cycles to determine if they correspond to the theoretical phases indicated by Eq. (3) with the phase parameter ϕ_0 set to 2722.762372-myr.

8.1. 7.398-gyr cycle

Of course, the largest cycle in this sequence, the 7.398-gyr cycle, is difficult to test by using spectral analysis because the astronomical data contains less than two repetitions. Because the UWS cycles seem to be quasi-periodic, we begin trusting spectral analysis results for data with five repetitions and have the greatest confidence for well-dated records with 20 or more repetitions.

Nonetheless, many of the time-series used as inputs for the spectra in Fig. 2 showed strong spectral density at frequencies corresponding to 6-to-9-gyr cyclicity. This was especially evident in the Mean Astronomical Activity Periodogram (an equally weighted average of the eight time-series used to generate the spectra in Fig. 2a–h). The 6-to-9-gyr range lies beyond the left edge of Fig. 2, but can be seen by the strong upward slope in the spectrum from the Mean Astronomical Activity Periodogram in Fig. 2i. However, in this particular case, the strongest evidence for the

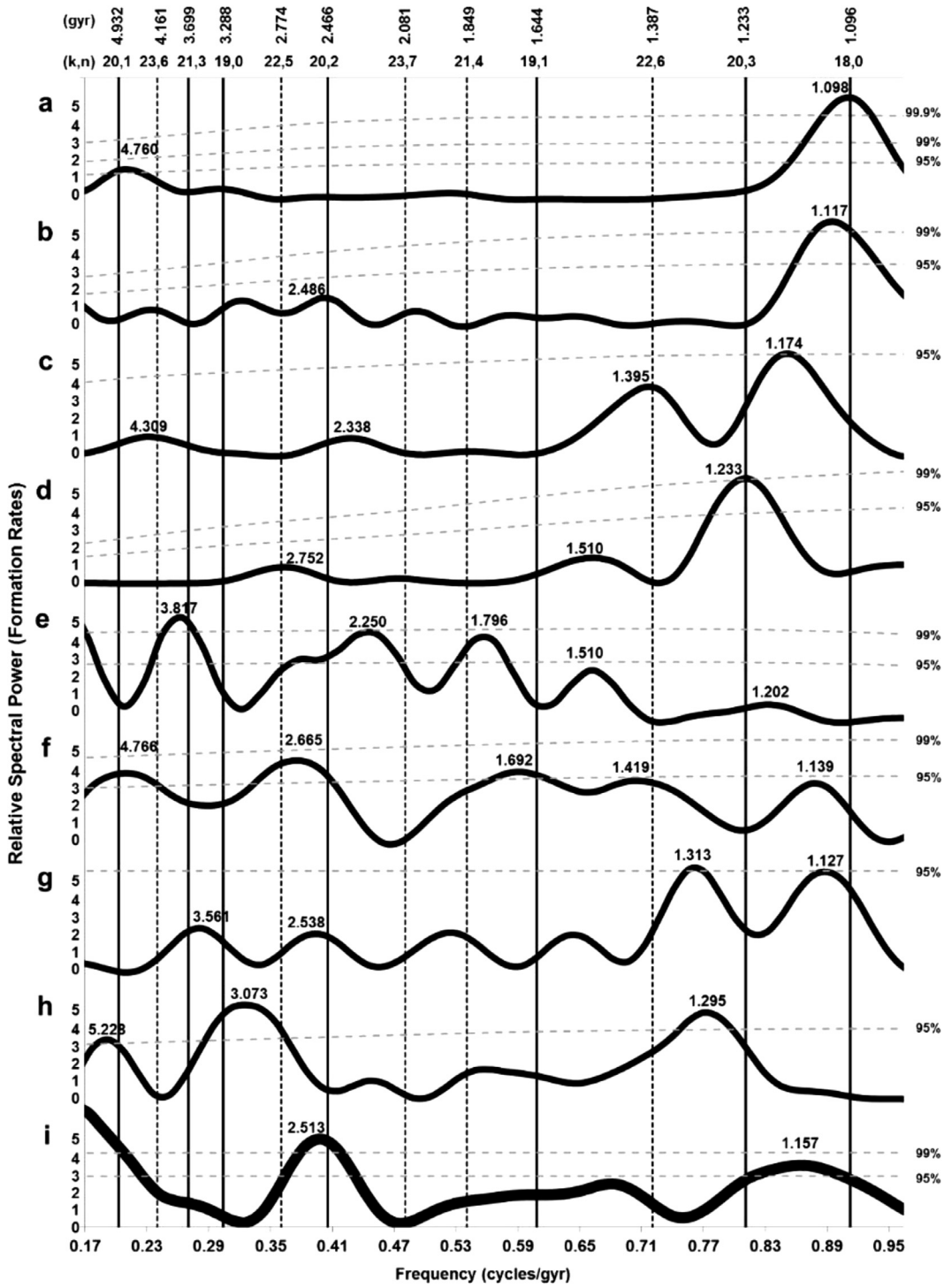

Fig. 2. Spectra showing cycles in astronomical events for the 1-gyr to 6-gyr bands, from filtered time-series records spanning the interval 13.7-0 Ga. Panel a—Solar region stars [37]. Panel b—Solar region stars [13]. Panel c—Solar region stars [5]. Panel d—Stars in globular clusters from nearby galaxies (*GC-1441 Dataset*). Panel e—SDSS quasars from SDSS-DR10 [2]. Panel f—Segue quasars from SDSS-DR10 [2]. Panel g—Gamma ray bursts (*GRB-397 Dataset*). Panel h—Supernovae from SDSS-II [47]. Panel i—Mean Astronomical Activity Periodogram, derived from the nine astronomical time-series displayed in Fig. 3.

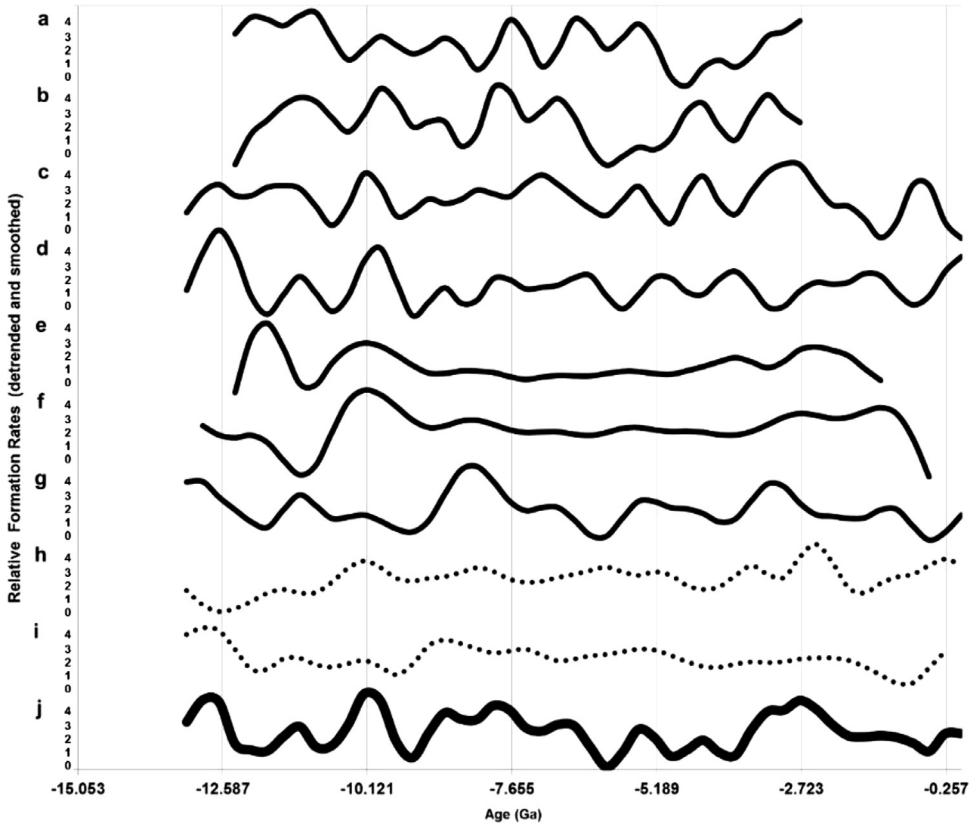

Fig. 3. Filtered and smoothed time-series plots of astronomical events for the interval 13.7-0 Ga. The vertical gridlines designate theoretical peaks of the 2.466-gyr $P_{20,2}$ cycle, calculated from Eq. (3). Panel a—Solar region stars [37]. Panel b—Solar region stars [13]. Panel c—Solar region stars [5]. Panel d—Stars in globular clusters from nearby galaxies (*GC-1441 Dataset*). Panel e—SDSS quasars from SDSS-DR7 [88]. Panel f—SDSS quasars from SDSS-DR10 [2]. Panel g—Segue quasars from SDSS-DR10 [2]. Panel h—Gamma ray bursts (*GRB-397 Dataset*). Panel i—Supernovae from SDSS-II [47]. Panel j—Mean astronomical activity time-series from panels a–i.

7.398-gyr cycle comes from the time-series plot in Fig. 3. Eq. (3) for the 7.398-gyr cycle indicates maximum astronomical formation at two times—10.121 billion years ago (Ga) and 2.723 Ga. Indeed, Fig. 3 shows that most of the astronomical time-series had heightened activity at these times, which also corresponded to the two largest peaks in the Mean Astronomical Activity time-series (Fig. 3j).

8.2. 2.466-gyr cycle

In addition to some evidence for the 7.398-gyr cycle, Figs. 2 and 3 also provide support for the 2.466-gyr $P_{20,2}$ cycle and the 1.233-gyr $P_{20,3}$ cycle. All of the spectra in Fig. 2 show a significant cycle in the 1.1-to-1.3-gyr range, but limited evidence for the 2.466-gyr cycle. Interestingly, the spectrum from the Mean Astronomical Activity periodogram in Fig. 2i shows the opposite—powerful evidence for the 2.466-gyr cycle (at the 99% confidence level) and reduced evidence of a 1.233-gyr cycle (with a peak at 1.157-gyr, at the 95% confidence level). Once again, the time-series plots add to the assessments of periodicity from Fig. 2 by illustrating the degree of alignment with the theoretical UWS peaks at 12.587, 10.121, 7.655, 5.189, 2.723, and 0.257 Ga, calculated from Eq. (3), and printed on the *x*-axis of Fig. 3. The formation times of quasars, GRBs, supernovae, globular clusters, and stars all primarily depend on age models of redshift measurements and/or metallic content.

Even though redshift measurements are as precise as radiometric measurements of rock ages, the models for converting the redshift values to gyr-ages remain uncertain. Likewise, a variety of models based on factors such as luminosity, rotation periods, and metallicity are used to assign ages to stars and globular clusters. The errors associated with these estimates are often as large as 25%. For instance, Holmberg et al. [37] (Fig. 3a) used the same dataset of solar-region stars as Casagrande et al. [13] (Fig. 3b), but the two research teams used different age models. Even though the times of maximum star formation were similar for both models, the amplitudes of the formation rates were noticeably different. In fact, the ages for the two models diverged so dramatically for the endpoints (ages greater than 12.4 Ga and less than 2.7 Ga) that we lost confidence in the estimates, and eliminated them from the time-series plot. Fig. 3c shows another sample of solar-region stars derived from yet another age-model [5].

Fig. 3e–g show quasar formation rates from three different surveys. Fig. 3h and i show the occurrences of stellar deaths (GRBs and supernovae). As might be expected, stellar deaths are roughly asynchronous to stellar births. Thus, Fig. 3h–i appear as dotted plots to indicate the records were inverted before placing them in the figure—an inversion convention used throughout this work. The scarcity of GRBs

Table 1
Time-lagged cross correlation results for the 2.466-gyr and 1.233-gyr UWS cycles.

Ref. fig.	Type of data	T. series range (Ga)	Model period (gyr)	T. lag CC +/- (gyr)	T. lag CC +/- (%mp)	T. lag CC+/- (rad)	No. of rep	Corr coef w/lag	Conf lvl (%)
3g	Segue survey of quasars	13.2–0.0	2.466	0.550	22.3%	1.40	5.4	0.28	80
3j	Mean astronomical activity	13.7–0.0	2.466	0.115	4.7%	0.29	5.6	0.47	99
3a	Solar-region stars	13.7–0.3	1.233	−0.509	−41.2%	−2.59	11	0.17	75
3c	Solar-region stars	13.7–0.0	1.233	0.349	28.3%	1.78	11	0.28	95
3d	Clusters in nearby galaxies	13.7–0.0	1.233	−0.059	−4.8%	−0.30	11	0.47	99.9

Notes: Ref. fig. is the figure and panel of the time-series plot. T. series range gives the beginning and ending ages for the time-series used in the lagged cross correlation. Model period is the UWS period used in the lagged cross correlation. T. lag CC +/- is the cross correlation lead/lag time given in (a) of billions of years (gyr), (b) as a percentage of the model period (%mp), and (c) in radians (rad). No. of rep is the number of repetition for the cycle during the T. series range. Corr coef w/lag is the Pearson correlation coefficient calculated after applying the lead/lag time T. lag CC +/- (gyr). Conf lvl (%) is determined from Monte Carlo simulations.

at the theoretical peaks of the 7.398-gyr cycle is visible in Fig. 3h from the two peaks at 10.121 Ga and 2.723 Ga. From this, it seems reasonable to state that theoretical peaks of the gyr-scale UWS cycles correspond to conditions favorable for stellar formation, while theoretical troughs of the UWS cycles correspond to conditions favorable for stellar destruction.

The Mean Astronomical Activity time-series in Fig. 3j best illustrates the interference pattern shown in Fig. 1e. In this instance, interference between the 1.233-gyr and 2.466-gyr cycles produces a sequence of stronger peaks at times marked by the vertical gridlines (designating 2.466-gyr maxima) and weaker peaks midway between the vertical gridlines. The same pattern is somewhat visible in formation plots in Fig. 3a–d, although each sample/age-model combination places the alternating peaks at slightly different times.

As mentioned, a time-series plot provides a subjective means for deciding if determinations about periodicity and the correctness of a model seem reasonable. In contrast, the periodograms give objective measurements about periodicity, while time-lagged cross correlation analyses give objective measurements of the degree of fit between the Eq. (3) model and the natural time-series records. In particular, when a periodogram indicates a cycle corresponding to a UWS frequency at a confidence level exceeding 95%, we want to know if the oscillations corresponded to the phases indicated by Eq. (3). This was accomplished by finding the lead-lag time between the time-series and the model, the Pearson correlation coefficient at the lead/lag time, and the confidence level that the correlation did not result from pure chance. We estimated the probability of chance causing the cycles from Monte Carlo methods—that is, by generating random number sequences with the same number of sample points as the real data, and then subjecting the random number sequences to identical tests as the real data. The Monte Carlo simulations showed that random number sequences can generate patterns closely resembling cyclicity with relatively high correlation coefficients, but only when there were a small number of repetitions. As the number of repetitions of a cycle increases, the probability of obtaining a high correlation coefficient from random sequences declines correspondingly. Thus, by itself, a Pearson correlation coefficient is meaningless. It must always be evaluated in terms of the number of sample points (or number of cycles) used in the test.

If the model given by Eq. (3) has validity, then the time-lagged cross correlation results should show a high concentration of lead/lag times in the first of four quartiles. The first quartile consists of deviations from the model-period of -12.5% to 12.5%, that is, with the absolute values of the deviations being less than 12.5% (0.785 rad); the second quartile with absolute values from 12.5% to 25% (0.785–1.571 rad); the third quartile with absolute values from 25% to 37.5% (1.571–2.356 rad); and the fourth quartile with absolute values from 37.5% to 50% (2.356–3.142 rad). Table 1 summarizes the time-lagged cross correlation results at the gyr-scale. Because of the relatively large uncertainty associated with some of the astronomical age models, the astronomical lead/lag times did not always correspond to the model as closely as expected. However, these were the exceptions.

At the gyr-scale, the best measurement of periodicity, the Mean Astronomical Activity time-series (Fig. 3g) gave strong evidence of the 2.466-gyr cycle—with the time-series leading the model by only 0.115-gyr (0.29 rad) at the 99% confidence level. Likewise, the time-lagged cross correlation for the 1.233-gyr cycle in globular clusters in nearby galaxies (Fig. 3d) lagged the model by only 0.059-gyr (−0.30 rad) at a 99.9% confidence level. This is important because if the results consistently show only small deviations between the natural records and the UWS model, then it indicates that the model (with every third repetition of a $P_{k,n}$ cycle aligning exactly with a $P_{k+1,n}$ cycle) has validity. Conversely, if the valid cycles are found to be scattered across all four quartiles, then the tests would indicate random distribution of the cycles—which would discredit the UWS model.

The tests associated with the 2.466-gyr cycle were strictly related to astronomical events. However, there is some indication of the cycle causing extreme geological and biological havoc. The catastrophic superplume event of ~2.723 Ga was so intense that it prompted Condie [16] to ask: What on Earth happened 2.7 billion years ago? This massive volcanism occurred near the first peak of the 2.466-gyr cycle after Earth formed – at 2.723 Ga. The second occurrence of the 2.466-gyr cycle occurred at ~257 Ma—closely coinciding with the "Great Dying" (end-Permian mass extinction). Shen et al. [91] described this mass extinction as the most severe biodiversity crisis in Earth history, and identified the timing of the event as 252 Ma—within 5-myr of the theoretical peak of the cycle. Of course, only two repetitions of the 2.466-gyr cycle

Table 2
Time-lagged cross correlation results for the 822-myr UWS cycle.

Ref. fig.	Type of data	T. series range (Ga)	Model period (myr)	T. lag CC +/- (myr)	T. lag CC +/- (%mp)	T. lag CC+/- (rad)	No. of rep	Corr coef w/lag	Conf lvl (%)
5c	Paleointensity (inverse)	3.6–0.0	822	351.6	42.8%	2.69	4.4	0.65	99.9
5d	Zircons	3.6–0.0	822	−24.0	−2.9%	−0.18	4.4	0.61	99.9
5e	Zircons	3.6–0.0	822	2.6	0.3%	0.02	4.4	0.49	99
5f	Mean geological activity	3.6–0.0	822	91.6	11.1%	0.70	4.4	0.59	99.9
5g	Mean astronomical activity	13.6–0.0	822	−6.9	−0.8%	−0.05	17.	0.16	80
5j	Solar-region stars	13.6–0.4	822	−43.3	−5.3%	−0.33	16.	0.24	95

Notes: Same column headings as in Table 1.

prevent rigorous testing of it with geological data. However, the extreme nature of the events at ~2700 Ma and 252 Ma indicate that the 2.466-gyr cycle might impact Earth significantly, and is deserving of further study.

8.3. 822-myr cycle

The analysis now focuses on the 822-myr $P_{19,2}$ cycle. At this scale, geological data become available for testing. However, similar to the astronomical data at the gyr-scale, the limited number of repetitions in the geological records, generally 4–5 repetitions of the cycle, places the geological results on the borderline for qualifying as valid tests.

The star formation records have adequate repetitions (~16 cycles), but the temporal resolution for the records from Casagrande et al. [13] (Fig. 4h) positions the time-series just within the Nyquist limit for evaluating the 822-myr cycle. Despite these limitations, the spectral analysis results (Fig. 4) show strong support for the 822-myr cycle—especially evident in paleointensity (Fig. 4c), zircon formation (Fig. 4d-e), globular cluster formation (Fig. 4f), and star formation (Fig. 4g–i). The results also provide moderate support for the 548-myr $P_{18,2}$ cycle—especially evident in the geomagnetic reversal rate (Fig. 4a and b).

The time-series plots (Fig. 5) also demonstrate considerable alignment with the UWS maxima designated by the vertical gridlines. The alignment is especially noticeable in the Mean Geological Activity time-series (Fig. 5f) and in the Mean Astronomical Activity time-series (Fig. 5g). The time-lagged cross correlation results (Table 2) also show agreement with the 822-myr UWS model. Even though both zircon datasets (Fig. 5d and e) have only 4.4 repetitions, they show almost perfect alignment with the model. The zircons from Voice et al. [106] only lag the model by 24.0-myr, with a 99.9% confidence level, while the zircons from Condie [17] lead the model by a 2.6-myr, with a 99% confidence level. The Mean Astronomical Activity time-series (Fig. 5g, consisting of star and globular cluster formation) lags the model by 6.9-myr, but only with an 80% confidence level.

The inverted paleointensity time-series (Fig. 5c) leads the 822-myr model by 351.6-myr (2.69 rad) and with a 99.9% confidence level. However, these results are somewhat suspect because the sampling was relatively poor for the interval 3600–1890 Ma. Nonetheless, at every timescale, the time-lagged cross correlation results for the inverted paleointensity index slightly led the model, but not to the extent of 2.69 rad. We interpret this as an inverse correlation with a slight lead time. Alternatively, it could be interpreted as a positive correlation with a long lag time. With inverse paleointensity being the exception, the other five tests in Table 2 were within the first quartile of deviations, with the absolute value of their deviations being less than 0.785 rad.

8.4. 274-myr cycle

The next set of periodograms (Fig. 6) supports the 274-myr $P_{18,2}$ cycle in the geomagnetic reversal rate (Fig. 6a and b), zircon formation (Fig. 6g), and star formation (Fig. 6h–i). The geomagnetic reversal records from [69] (Fig. 6d) and the paleointensity records in the PINT-2014 database (Fig. 6e) were supportive of the 182.7-myr $P_{17,2}$ cycle. The Nyquist limit prevented detection of star formation cycles with periods less than 200-myr. With the exception of the paleointensity time-series, all of the geological time-series also indicated a cycle very close to the 137-myr $P_{18,3}$ cycle.

The plots for the interval 4093-0 Ma (Fig. 7) show moderately close phase relationships between each time-series and the 274-myr UWS model (with peaks designated by the vertical gridlines). The synchronous 274-myr phase relationships between star formation and geological activity is especially evident in the Mean Geological Activity time-series (Fig. 7g) and the Mean Star Formation time-series (Fig. 7h) from 3545 Ma to 1901 Ma.

Table 3 summarizes the time-lagged cross correlation results. The geomagnetic reversal rates (Fig. 5a and b) lagged the 548-myr model by 36.5-myr and 42.5-myr respectively (both less than 0.50 rad from an exact match). The geomagnetic reversal rate in Fig. 7b also lagged the 274-myr model, but by only 28.5-myr (-0.65 rad). The combination of tests indicates that every second oscillation of the 274-myr cycle contributes to greater frequency in geomagnetic reversals—seen at ages of 3271, 2723, 2175, 1627, 1079, and 531 Ma in Fig. 7a–c. Zircons (Fig. 7f) and the Mean Geological Activity time-series (Fig. 7g) again demonstrate near-perfect correlations with a $P_{k,2}$ model (the 274-myr cycle) with zircons lagging the model by 14.9-myr (-0.34 rad) at a 99% confidence level, and the Mean Geological Activity time-series leading the model by 3.6-myr (0.08 rad). The star formation time-series (Fig. 7h–i) aligned well with the model since 4093 Ma, but became asynchronous for older ages—possibly indicating the limits for this type of analysis because of the large age errors for their age-models.

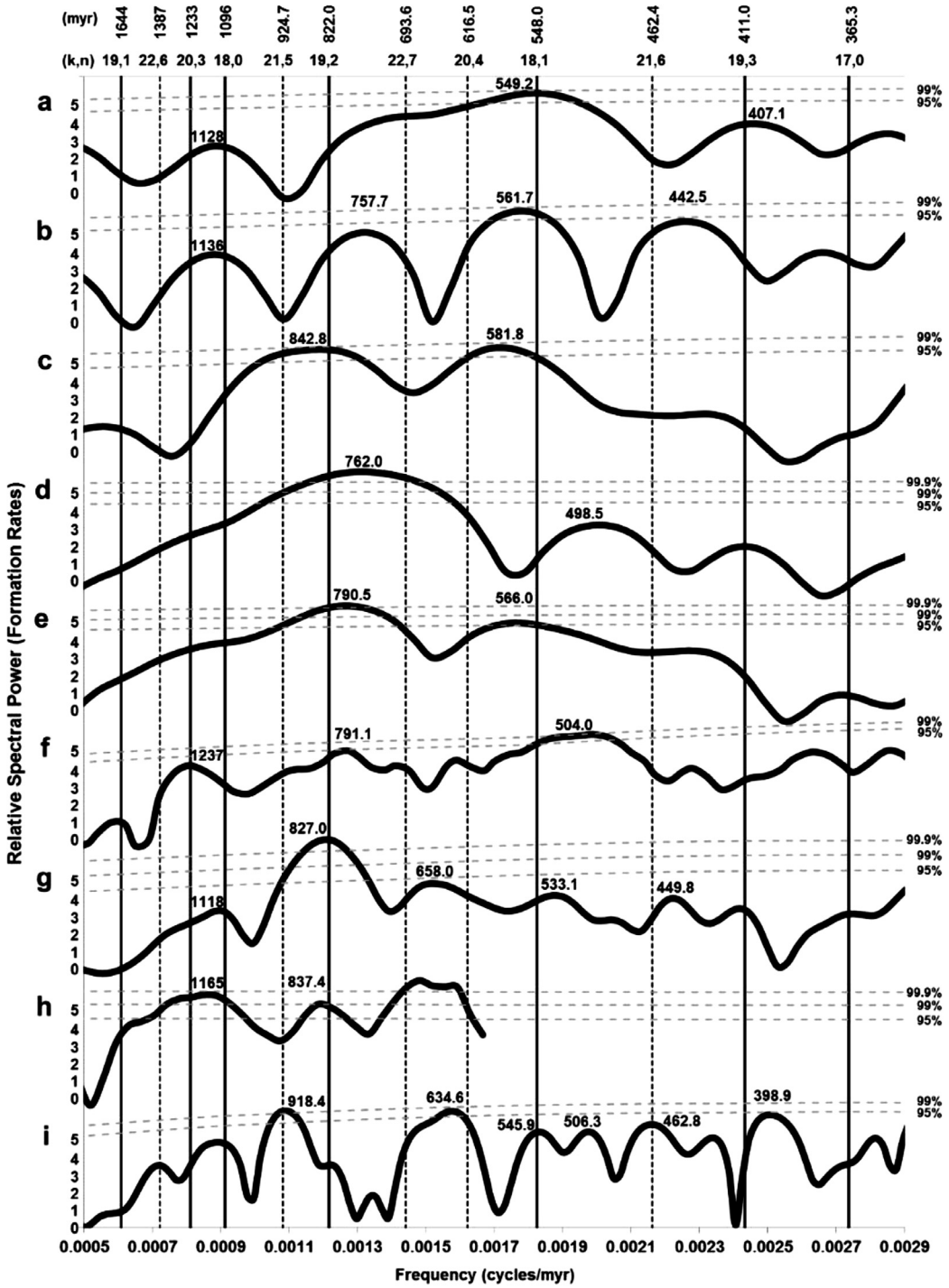

Fig. 4. Spectra of the geomagnetic reversal rate, paleointensity, zircon formation, and star formation in the 350-myr to 2000-myr bands, from filtered time-series records spanning the interval 13.6-0 Ga for stars but only from 3.6-0 Ga for geological records. Panel a—Composite time-series of the geomagnetic reversal rate [28,103]. Panel b—Geomagnetic reversal rate [78]. Panel c—Paleointensity [10]. Panel d—Zircon formation rate [106]. Panel e—Zircon formation rate [17]. Panel f—Globular cluster stars from nearby galaxies (*GC-1441 Dataset*). Panel g—Solar region stars [37]. Panel h—Solar region stars [13]. Panel i—Solar region stars [5].

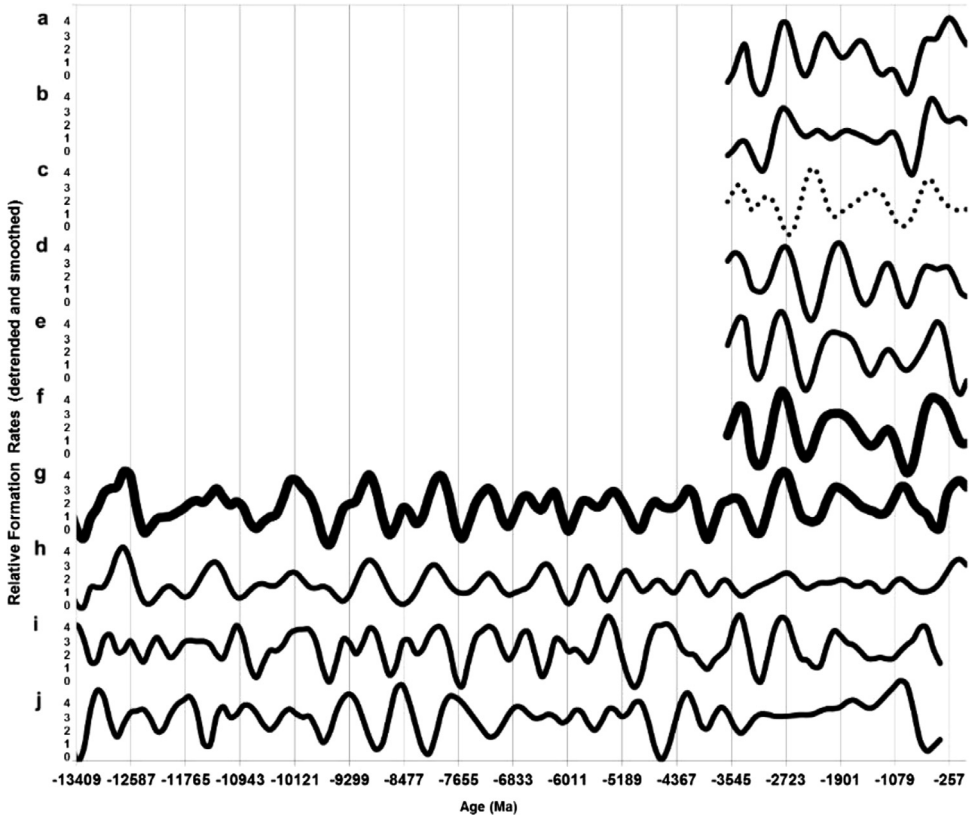

Fig. 5. Filtered and smoothed time-series plots of the geomagnetic reversal rate, paleointensity, zircon formation, and star formation for the interval 13409-0 Ma. The vertical gridlines designate theoretical peaks of the 822-myr $P_{19,2}$ cycle, calculated from Eq. (3). Panel a—Composite time-series of the geomagnetic reversal rate [28,103]. Panel b—Geomagnetic reversal rate [78]. Panel c—Paleointensity [10]. Panel d—Zircon formation rate [106]. Panel e—Zircon formation rate [17]. Panel f—Mean geological time-series from panels a–e. Panel g—Mean star formation time-series from panels h–j. Panel h—Globular clusters from nearby galaxies (*GC-1441 Dataset*). Panel i—Solar region stars [5]. Panel j—Solar region stars [37].

Table 3
Time-lagged cross correlation results for the 548-myr and 274-myr UWS cycles.

Ref. fig.	Type of data	T. series range (Ga)	Model period (myr)	T. lag CC +/- (myr)	T. lag CC +/- (%mp)	T. lag CC+/- (rad)	No. of rep	Corr coef w/lag	Conf lvl (%)
5a	Geomagnetic reversal rate	3.6–0.0	548	−36.5	−6.7%	−0.42	6.6	0.31	90
5b	Geomagnetic reversal rate	3.6–0.0	548	−42.5	−7.8%	−0.49	6.6	0.42	99
7b	Geomagnetic reversal rate	3.5–0.0	274	−28.5	−10.4%	−0.65	13.	0.35	99
7f	Zircons	3.5–0.0	274	−14.9	−5.4%	−0.34	13.	0.38	99
7g	Mean geological activity	3.5–0.0	274	3.6	1.3%	0.08	13.	0.48	99.9
7h	Mean astronomical activity	13.6-0.4	274	106.9	39.0%	2.45	48.	0.14	95
7i	Solar-region stars	13.6–0.4	274	131.7	48.1%	3.02	48.	0.10	85

Notes: Same column headings as in Table 1.

8.5. 91.33-myr cycle

The next tests span the interval from 1390 Ma to present—ages where the temporal resolution for geological data remains sufficient for analyzing cycles in bands below 200-myr. The only astronomical data with sufficient temporal resolution (the globular clusters from the GC-1441 Dataset) showed strong spectral power (Fig. 8a) near the frequency corresponding to the 91.33-myr $P_{17,2}$ cycle.

Additionally, every geological time-series in Fig. 8 indicated similar periodicity. The spectrum for zircon formation from Voice et al. [106] showed exceptional power near 91.33-myr—far above the 99.9% confidence level. Likewise, spectra for the geomagnetic reversal rate (Fig. 8b and c) showed peaks almost identical to the 91.33-myr cycle with both attaining confidence levels above 99.9%.

The time-series plots in Fig. 9 show similar uniformity among the various geological proxies. The data for the

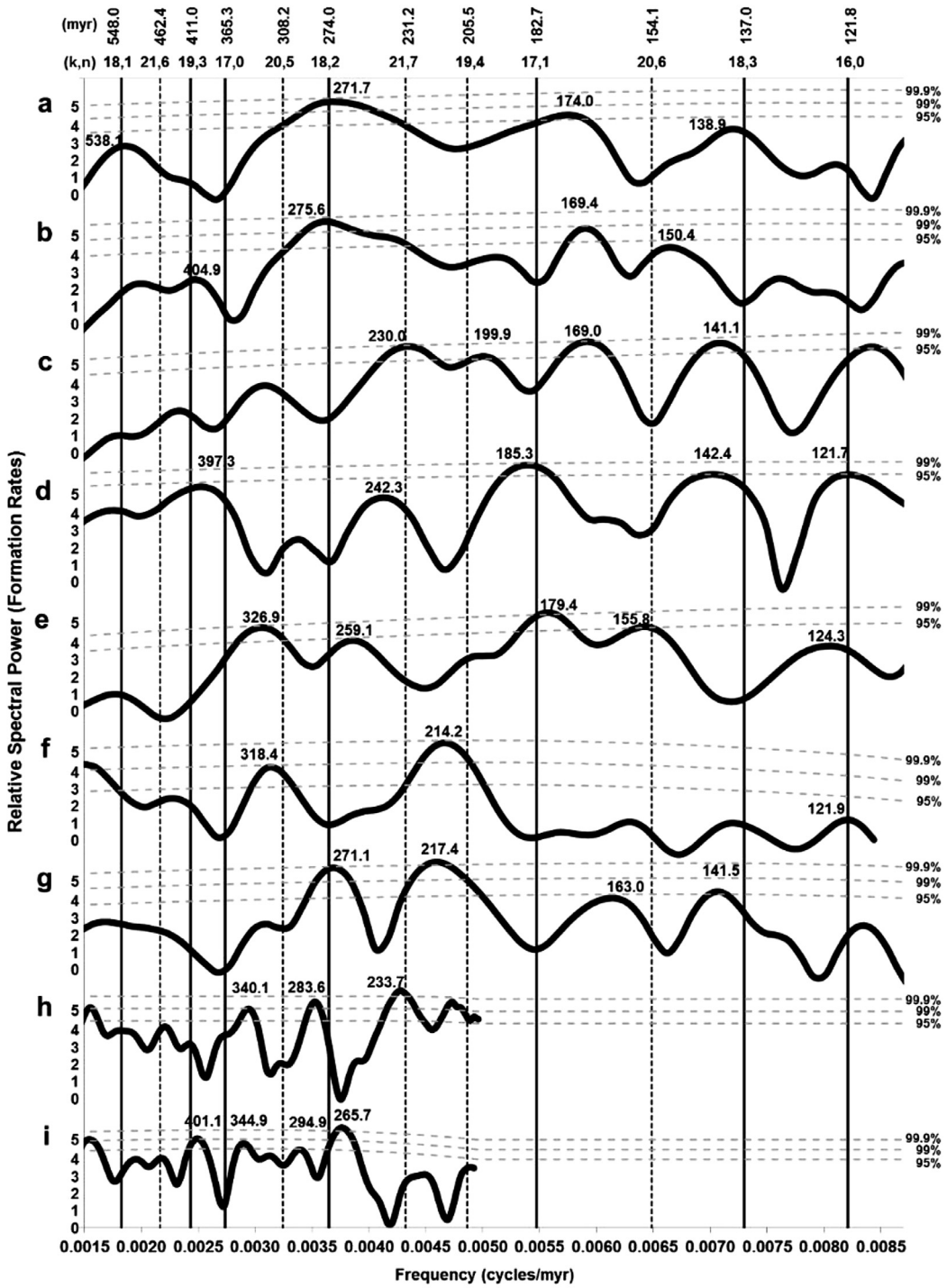

Fig. 6. Spectra of the geomagnetic reversal rate, paleointensity, zircon formation, and star formation in the 120-myr to 660-myr bands, from filtered time-series records spanning the interval 13.6-0 Ga for stars and 3.51-0 Ga for geological records. Panel a—From a composite time-series of the geomagnetic reversal rate [70,103]. Panel b—From a composite time-series of the geomagnetic reversal rate [28,103]. Panel c—Geomagnetic reversal rate [78]. Panel d—Geomagnetic reversal rate [69]. Panel e—Paleointensity [10]. Panel f—Zircon formation rate [106]. Panel g—Zircon formation rate [17].Panel h—Solar region stars [37]. Panel i—Solar region stars [5].

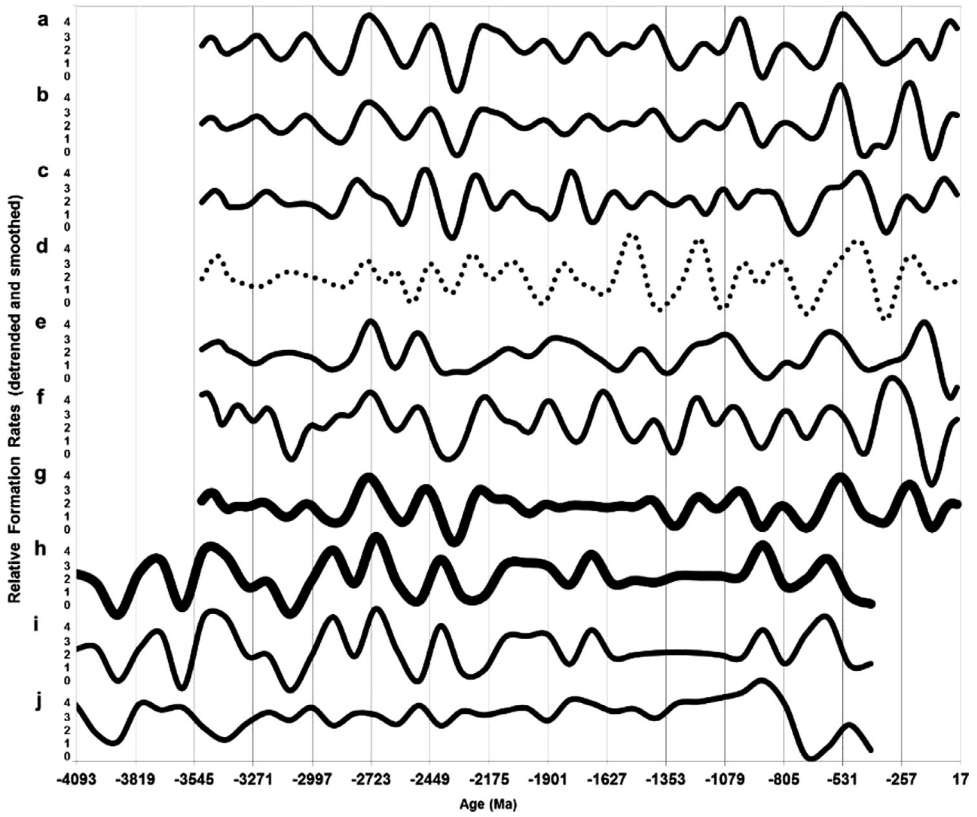

Fig. 7. Filtered and smoothed time-series plots of the geomagnetic reversal rate, paleointensity, zircon formation, and star formation for the interval 4093-0 Ma. The vertical gridlines designate theoretical peaks of the 274-myr $P_{18,2}$ cycle, calculated from Eq. (3). Panel a—Composite time-series of the geomagnetic reversal rate [70,103]. Panel b—Composite time-series of the geomagnetic reversal rate [28,103]. Panel c—Geomagnetic reversal rate [78]. Panel d—Paleointensity [10]. Panel e—Zircon formation rate [106]. Panel f—Zircon formation rate [17]. Panel g—Mean geological activity time-series from panels a–f. Panel h—Mean star formation time-series from panels i and j. Panel i—Solar region stars [5]. Panel j—Solar region stars [37].

interval from 1390 Ma to present are among the most reliable in this study because of the heavy sampling during these times (generally giving good temporal resolution) and the more reliable age estimates for younger events. Consequently, these tests deserve greater weighting when drawing conclusions. Thus, the apparent inverse correlation between paleointensity (dotted curve in Fig. 9e) and the other geological time-series seems warranted. Notice the near-perfect alignment for the geological records in Fig. 9b–h to the 91.33-myr maxima at 622, 531, 439, 348, 257, 165, and 74 Ma—calculated from Eq. (3).

The time-lagged cross correlations in Table 4 give results similar to the previous tests. The inverted paleointensity time-series (Fig. 7d and e) leads the 91.33-myr model, the zircon time-series (Fig. 9f–g) closely coincide with the model, the geomagnetic reversal rates (Figs. 6d, 9b–d) tend to lag the model slightly, and the Mean Geological Activity time-series almost perfectly matches the model—lagging by only 0.36-myr (-0.02 rad) with a 99.99% confidence level.

8.6. 30.44-myr cycle

For some of the data, the resolution deteriorates to the point where meaningful tests are impossible at scales below 60-myr. Other than the quasar data, none of the astronomical records meet the temporal resolution requirements for testing the 30.44-myr $P_{16,2}$ cycle. Similarly, the periodograms for the geomagnetic reversal rate in Fig. 10 show noticeable differences. Fig. 10a and d show evidence of a 30.44-myr cycle in the reversal rate, while Fig. 10b and c do not.

However, the combined records from Gradstein et al. [28] and Veikkolainen et al. [103] have the largest number of samples and contain the latest estimates of geomagnetic reversals and must be considered the best estimates at this time. The periodogram for this time-series (Fig. 10b) and the estimate from Pechersky [69] show strong periodicity near the 15-myr (15.22-myr UWS) and 30-myr (30.44-myr UWS) harmonics initially postulated by Mazaud et al. [57] and Stothers [95] and mentioned in Section 1. As usual, the heavily sampled zircon datasets (Fig. 10f and g) demonstrate exceptional spectral power near the $P_{k,2}$ cycle—this time, validating the 30.44-myr $P_{16,2}$ cycle.

Fig. 11 has plots for the geomagnetic reversal rate (Fig. 11a–d), inverted paleointensity (Fig. 11e), zircons (Fig. 11f–g), and the Mean Geological Activity time-series (Fig. 11h) where the 30.44-myr cycle is most evident. The panels in Fig. 11 also show the period-tripling pattern of the 91.33-myr cycle—with greater amplitudes near 531, 439, 348, 257, 165, and 74 Ma.

The time-lagged cross correlation results in Table 5 show tendencies similar to the results from the other timescales. The zircon correlations (Fig. 11f–g) and the Mean

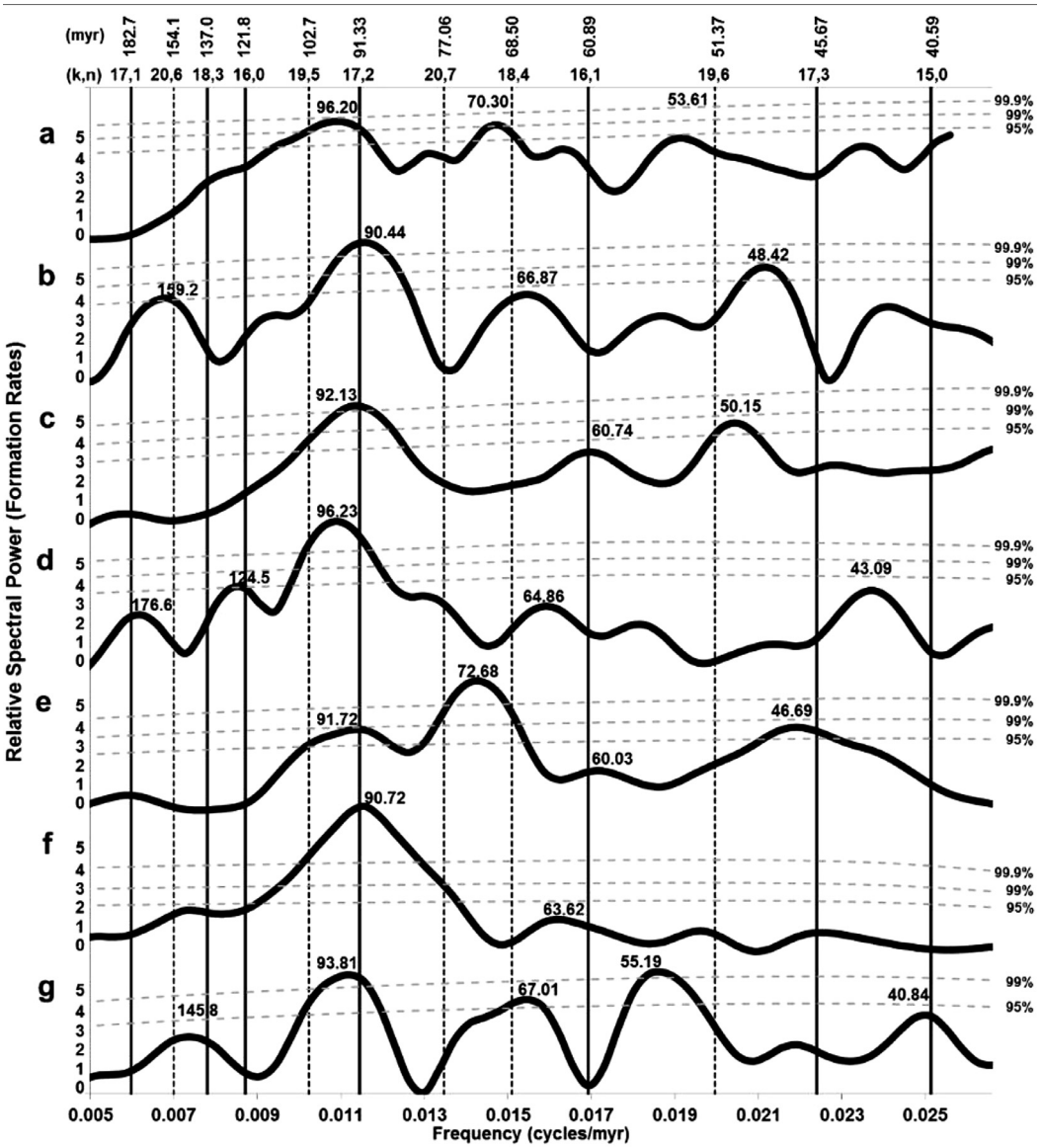

Fig. 8. Spectra of star formation, geomagnetic reversal rate, paleointensity, and zircon formation in the 38-myr to 200-myr bands, from filtered time-series records spanning the interval 1390-0 Ma. Panel a—Globular cluster stars from nearby galaxies (*GC-1441 Dataset*). Panel b—From a composite time-series of the geomagnetic reversal rate [28,103]. Panel c—Geomagnetic reversal rate [78]. Panel d—Geomagnetic reversal rate [69]. Panel e—Paleointensity [10]. Panel f—Zircon formation rate [106]. Panel g—Zircon formation rate [17].

Geological Activity time-series (Fig. 11h) are mostly synchronous with the 30.44-myr UWS model, while the geomagnetic reversal rate (Fig. 11d) tends to lag the model slightly—in this instance, lagging the model by quite a bit at 6.748-myr (−1.39 rad).

9. Discussion

The results showed 33 instances of a periodogram with evidence of a UWS cycle, and the time-lagged cross correlation tests indicated the cycles were non-random, at a confidence level above 70%. Most of these tests involved cycles in the $P_{k,2}$ sequence from Eq. (1). The tests involved four types of data: astronomical, volcanic, paleointensity, and geomagnetic reversal rates.

We placed the residuals (deviations) from the UWS model into one of four quartiles—with the first quartile containing residuals in close proximity to the phases of the model, with the residuals becoming progressively less synchronous as the quartiles increased, and with the fourth quartile containing residuals roughly asynchronous to the phases of the model. If the aforementioned processes are synchronous with the UWS model, then the residuals should be concentrated in the first quartile. However, if the processes are random, then the residuals should be scattered evenly among the four quartiles.

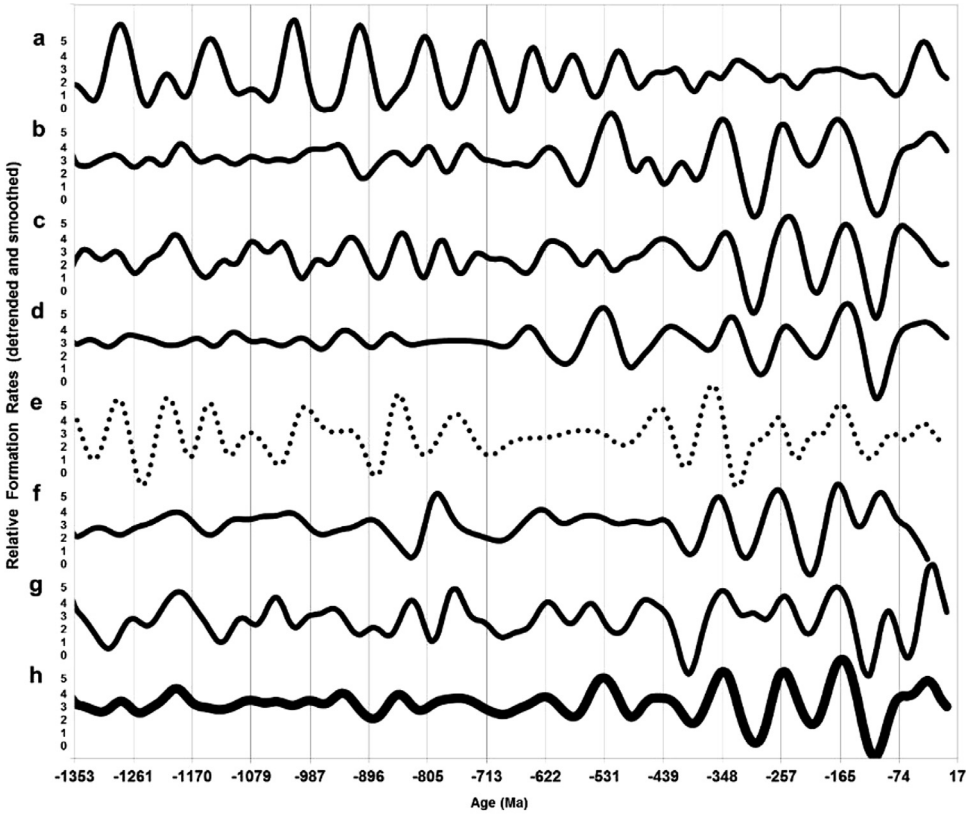

Fig. 9. Filtered and smoothed time-series plots of star formation, geomagnetic reversal rate, paleointensity, and zircon formation for the interval 1353-0 Ma. The vertical gridlines designate theoretical peaks of the 91.33-myr $P_{17,2}$ cycle, calculated from Eq. (3). Panel a—Globular cluster stars from nearby galaxies (*GC-1441 Dataset*). Panel b—Composite time-series of the geomagnetic reversal rate [28,103]. Panel c—Geomagnetic reversal rate [78]. Panel d—Geomagnetic reversal rate [69]. Panel e—Paleointensity [10]. Panel f—Zircon formation rate [106]. Panel g—Zircon formation rate [17]. Panel h—Mean geological activity time-series (panels a–g).

Table 4
Time-lagged cross correlation results for the 182.7, 91.33, and 45.67-myr UWS cycles.

Ref. fig.	Type of data	T. series range (Ma)	Model period (myr)	T. lag CC +/- (myr)	T. lag CC +/- (%mp)	T. lag CC+/- (rad)	No. of rep	Corr coef w/lag	Conf lvl (%)
6d	Geomagnetic reversal rate	1740–0	182.7	10.79	5.9%	0.37	10	0.45	99.9
7d	Paleointensity (inverse)	3510–0	182.7	79.42	43.5%	2.73	19	0.25	99
9a	Clusters in nearby galaxies	1390–0	91.33	7.70	8.4%	0.53	15	0.15	70
9b	Geomagnetic reversal rate	1390–0	91.33	−13.67	−15.0%	−0.94	15	0.24	95
9c	Geomagnetic reversal rate	1390–0	91.33	−18.14	−19.9%	−1.25	15	0.18	85
9d	Geomagnetic reversal rate	1390–0	91.33	−17.18	−18.8%	−1.18	15	0.25	95
9e	Paleointensity (inverse)	1390–0	91.33	21.17	23.2%	1.46	15	0.30	99
9f	Zircons	1390–0	91.33	−7.15	−7.8%	−0.49	15	0.24	95
9g	Zircons	1390–0	91.33	4.86	5.3%	0.33	15	0.20	90
9h	Mean geological activity	1390–0	91.33	−0.36	−0.4%	−0.02	15	0.39	99.9
11e	Paleointensity (inverse)	1390–0	45.67	5.38	11.8%	0.74	30	0.09	70

Notes: Same column headings as in Table 1.

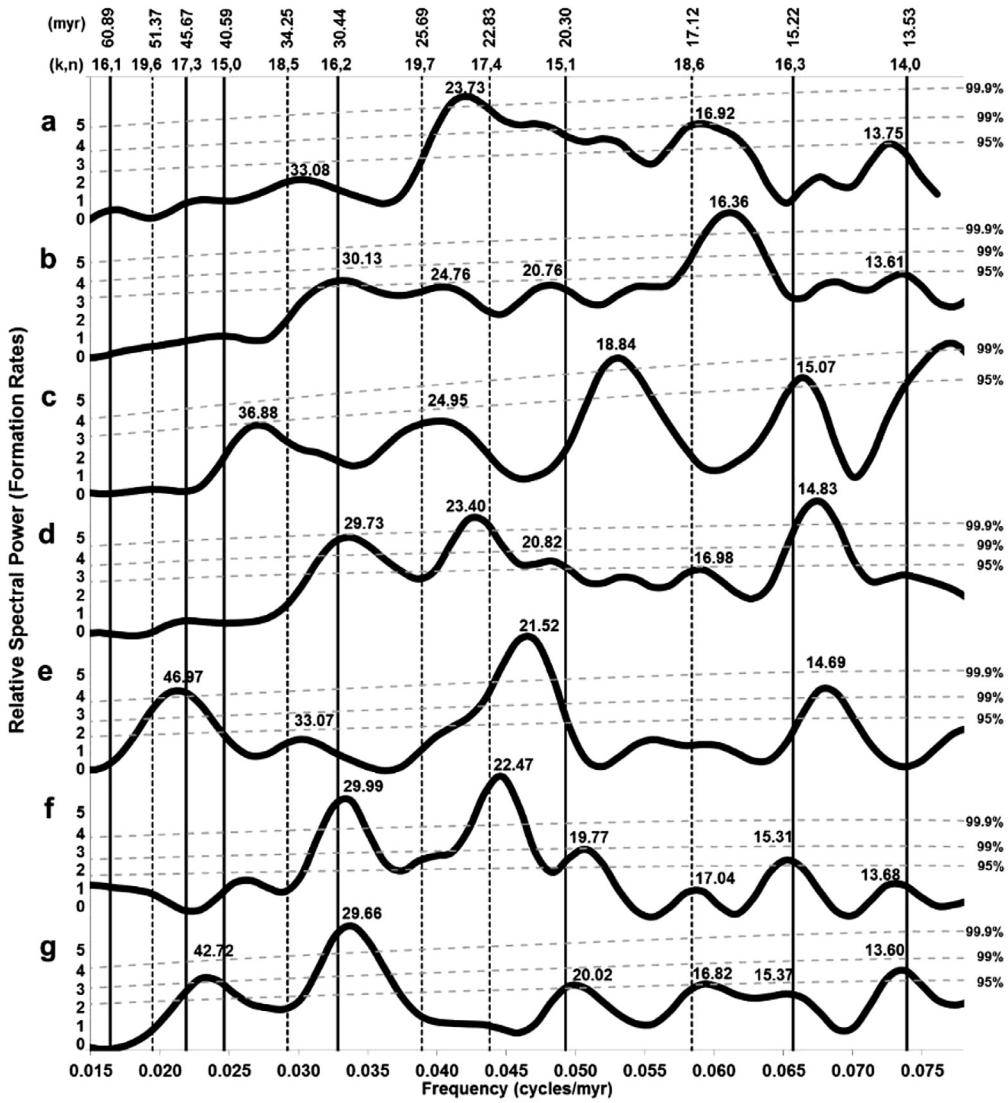

Fig. 10. Spectra of the geomagnetic reversal rate, paleointensity, and zircon formation in the 13-myr to 66-myr bands, from filtered time-series records spanning the interval 693-0 Ma. Panel a—From a composite time-series of the geomagnetic reversal rate [70,103]. Panel b—From a composite time-series of the geomagnetic reversal rate [28,103]. Panel c—Geomagnetic reversal rate [78]. Panel d—Geomagnetic reversal rate [69]. Panel e—Paleointensity [10]. Panel f—Zircon formation rate [106]. Panel g—Zircon formation rate [17].

The residuals from all 11 tests of zircon formation and the Mean Geological Activity time-series fell into the first quartile. In fact, 8 of the 11 residuals fell into the first half of the first quartile—indicating an unusually high correlation with the UWS model. The mean residual of these 11 tests was +0.013 rad—indistinguishable from perfect alignment with phases indicated by Eq. (3).

The residuals from the eight tests of the geomagnetic reversal rate all fell into the first two quartiles, with four in the first quartile and four in the second quartile. The mean residual was -0.74 rad, which fell inside the first quartile, but indicates that the geomagnetic reversal rate lags the UWS model slightly.

The residuals from the four tests of PINT-2014 paleointensity were scattered. One fell in the first quartile, one in the second quartile, and two in the fourth quartile. In all likelihood, paleointensity cycles are related to the other geological cycles, but we could not conclusively confirm that with the tests here. The sampling frequency was questionable for the pre-Cambrian era. However, the PINT-2014 database contained good temporal resolution for the Phanerozoic era, and the test from that portion of the time-series indicated an inverse correlation with the UWS model, with paleointensity leading the model by +0.74 rad.

Five of the residuals from the astronomical tests fell into the first quartile, and the other five residuals were scattered in the other three quartiles. Overall, the tests indicated that astronomical formations (such as births of stars, star clusters, and quasars) develop synchronously with the UWS model and with zircon formation on Earth.

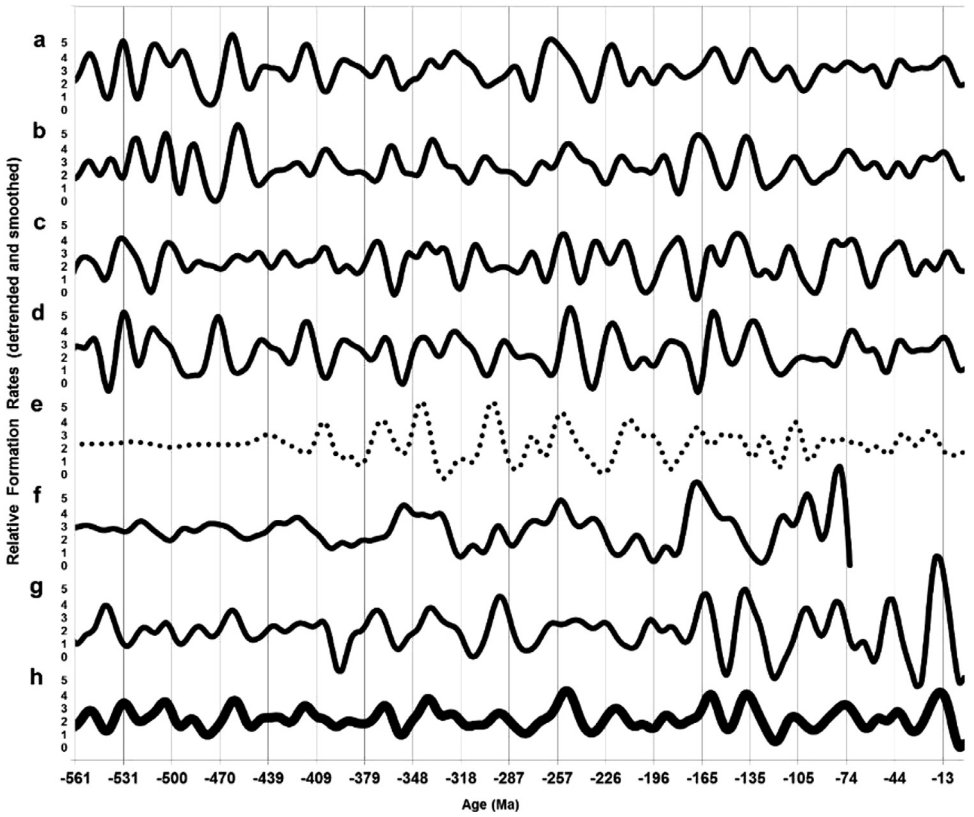

Fig. 11. Filtered and smoothed time-series plots of the geomagnetic reversal rate, paleointensity, and zircon formation for the interval 561-0 Ma. The vertical gridlines designate theoretical peaks of the 30.44-myr $P_{16,2}$ cycle, calculated from Eq. (3). Panel a—Composite time-series of the geomagnetic reversal rate [70,103]. Panel b—Composite time-series of the geomagnetic reversal rate [28,103]. Panel c—Geomagnetic reversal rate [78]. Panel d—Geomagnetic reversal rate [69]. Panel e—Paleointensity [10]. Panel f—Zircon formation rate [106]. Panel g—Zircon formation rate [17]. Panel h—Mean geological activity time-series (panels a–g).

Table 5
Time-lagged cross correlation results for the 30.44-myr UWS cycles.

Ref. fig.	Type of data	T. series range (Ma)	Model period (myr)	T. lag CC +/- (myr)	T. lag CC +/- (%mp)	T. lag CC+/- (rad)	No. of rep	Corr coef w/lag	Conf lvl (%)
11d	Geomagnetic reversal rate	693–0	30.44	−6.748	−22.2%	−1.39	23	0.17	90
11f	Zircons	693–0	30.44	3.262	10.7%	0.67	23	0.24	99
11g	Zircons	693–0	30.44	−1.332	−4.4%	−0.27	23	0.25	99
11h	Mean geological activity	693–0	30.44	−1.728	−5.7%	−0.36	23	0.29	99.9

Notes: Same column headings as in Table 1.

Conversely, astronomical deformations (such as deaths of stars) develop asynchronously with the UWS model. The astronomical conclusions are statistically less certain than the synchronous correlation between the UWS model and zircon formation. Some of the astronomical records contain ages from models still undergoing rapid development. The progress in developing these age-models is commendable, but it might take several more years before the ages assigned to astronomical formations achieve the same level of certainty as the radiometric dating of geological events.

The zircon results presented here are somewhat unsurprising because others have already identified many of the periods of maximum geological activity. For instance, more than 20 years ago, episodes of rapid crustal formation were estimated to have occurred at approximately 900-myr intervals at 3600, 2700, and 1800 Ma [59]. This was the first evidence of geological periodicity being in sync with the 822-myr UWS cycle. Then, Condie and Aster [18] and Voice et al. [106] found high rates of zircon formation at 3000, 2700, 1870, 1100–1000, 600, and 300–200 Ma. These ages approximately correspond to all of the 822-myr peaks since 3000 Ma and some of the 274-myr peaks given by Eq. (3). Condie [17] noted that although it is now well established that U/Pb ages from zircons show an episodic distribution and are associated with the supercontinent cycle, the reasons for these episodes are still not understood and are still subject

to ongoing debate. Condie et al. [19] suspect that mantle plume episodes are tied to the generation of continental crust. If so, then the zircon age distributions likely record the intensity of these events. However, the processes within the mantle that cause the geodynamic instabilities that initiate the plumes remain a mystery.

Korenaga [49] suggested that the supercontinent cycle was actually ~800-myr after considering Gondwanaland as a building-block for the more complete Pangea supercontinent. In this scenario, Korenaga [49] considered the complete set of supercontinents as Kenorland (2700–2600 Ma), Nuna (1800–1700 Ma), Rodinia (1100–1000 Ma), and Pangea (300–200 Ma)—again, ages consistent with maxima in crustal formation, zircon formation, and the 822-myr $P_{19,2}$, cycle.

The results from the astronomical and geomagnetic tests add to these previous discoveries by indicating that cycles in geomagnetic reversals and astronomical formations are related to zircon formation and the supercontinent cycle. By using a box counting method, Prokoph and Puetz [79] demonstrated that the geological patterns are indeed fractal, and suggested that the periodicity indicates the propagation of large-scale waveforms. The finding that geomagnetic reversals are related to zircon formation adds to the evidence of large-scale waveforms because periodic reversed motion is one of the primary properties of ordinary compression waves. The evidence indicates that the suspected waves are massive because the geological formations exhibit periods of 91.33, 274, and 822-myr that occur along with astronomical counterparts. This implies that the waves must extend over enormous astronomical regions to cause synchronous formations throughout the observed regions of the universe.

10. Theoretical assumptions, causality, and predictions

To this point, the Universal Cycle model and the UWS cycles that it describes [80,79] was empirical. Here, we speculate on a possible cause of the cycles, while explaining our reasoning, and making testable predictions based on the theory.

Because of the novelty of the Universal Cycle model, it is impossible to include every detail of every aspect of the hypothesis. Here, the summarization primarily focuses on aspects of the theory that pertain to volcanism, geomagnetic reversals, star formation, quasar formation, and galaxy formation.

The hypothesis is based on a fractal model of the universe, and it uses the equations commonly used to describe the motions of matter, such as gravitational equations, Newton's laws of motion, thermodynamics, fluid dynamics, and wave mechanics. New unexpected astronomical observations [45,46,52] also influenced decisions about formulating the hypothesis, as did the properties associated with the UWS cycles.

10.1. Deductive reasoning

Some properties of the universe are impossible to absolutely prove or disprove. For instance, is the universe finite or infinite? If the universe is finite, we cannot go to a potential edge of the universe to find a conclusive answer. And if the universe is infinite, we will not find an edge regardless of how long we search. When absolute proof is impossible, one can use deductive reasoning to determine what is likely to be true. In the process of deduction, one begins with premises that are assumed to be true, and then determines what else must be true if the premises are true. In this way, it is possible to absolutely prove or disprove a hypothesis, given that the original assumptions are indeed true. However, the assumptions themselves remain unproven and unprovable.

Thus, original assumptions only serve as a means for scientific exploration, and the assumptions can only be accepted as true to the degree to which they minimize or eliminate (a) discrepancies with accepted observations and (b) internal discrepancies within the theoretical framework of the model. Deductive reasoning involves valid logical methods, and it differs from the invalid logic of circular reasoning. However, one must be cautious because deductive reasoning can become circular if confirmation of a hypothesis is then inappropriately used as some sort of proof of the underlying assumptions.

10.2. Theoretical assumptions

Even though they cannot be absolutely proved or disproved, the following assumptions were treated as truths while formulating the Universal Cycle hypothesis. Thus, for deductive reasoning purposes:

Infinite universe—The universe is assumed to be infinite, and contains both infinitely large and infinitely small objects.

Fractal matter—All matter within the universe is assumed to develop fractally. That is, each piece of matter is assumed to be part of a self-similar larger object—as well as consisting of self-similar smaller objects.

Sub-electron fractal matter—Based on these assumption, there must be an infinite sea of miniscule matter, heretofore referred to collectively as sub-electron fractal (SEF) matter, in the form of a gas, that fills the regions of the universe previously considered as empty space. Of course, humans are unable to see any type of gas. Researchers only learned about the properties of various atomic and molecular gases from ingenious experiments. Likewise, we assume that the gaseous-like SEF matter can only be detected and measured from experiments—such as the periodograms and time-series plots used in this study.

Open systems—All objects in the universe are assumed to be part of an open system. That is, there are no perfectly closed systems. For instance, many of the properties of Earth and its atmosphere can be explained internally by its mass, core, rotational velocity, and atmospheric composition. However, external factors such as solar radiation, the solar wind, occasional bolide impacts, explosions from nearby supernovae, etc., are required to explain other events on Earth. It is assumed that events occur on (and within) all objects that involve both the internal matter of the object and interactions with different types of matter in the surrounding environments.

Relativism—All matter and the associated motions are assumed to have some similarities with other matter, as well as some dissimilarities—with each object in the universe assumed to be unique. The self-similarity of fractals permits idealized classifications of matter, such as oxygen atoms, main-sequence Class A stars, terrestrial plants, type Sa1

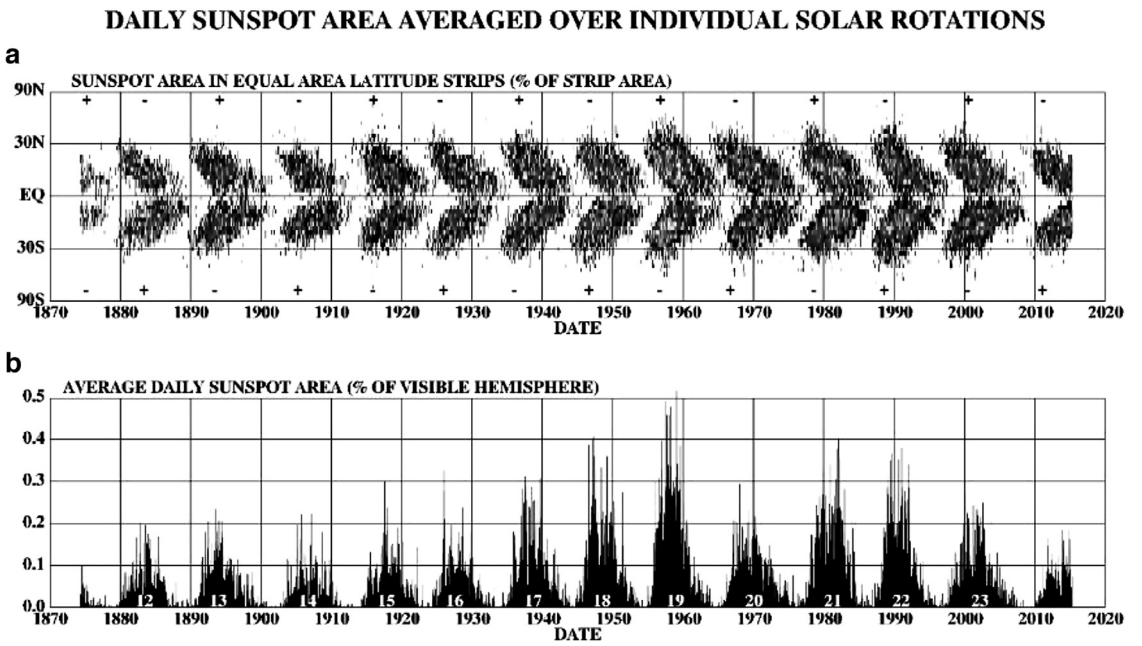

Fig. 12. Adapted from Hathaway, DH [33], with solar polarity labels (+/– signs) added here. (a) Latitude of sunspot areas, as a function of time, produces the so-called butterfly diagram. (b) Average daily sunspot numbers since 1875.

spiral galaxies, etc. Although each classification of matter has different components and properties, it is assumed that in a fractal universe, the self-similarities allow making reasonable deductions about the unknown properties of matter at one scale based on the known properties of matter at another scale.

Wave mechanics—We assume that the various divisions of gaseous SEF-matter serve as media for the propagation of the UWS cycles. Moreover, based on their properties, the UWS waves appear to follow the same rules as ordinary mechanical waves. All of us are familiar with mechanical waves in which atoms and/or molecules act as the medium—such as sound waves, water waves, or seismic waves. Other than a different medium (SEF-matter versus molecular matter) all rules associated with the propagation of the waves are assumed to be the same.

10.3. Butterfly diagram

A butterfly diagram (Fig. 12a) illustrates periodic patterns in the latitudes of sunspot areas—which appear as a sequence of butterflies, and thus the name of the diagram. Interestingly, the direction of solar flare loops reverses with every new solar cycle. Thus, the Sun also experiences magnetic reversals, but on a much shorter time-scale than on Earth. The top of Fig. 12a indicates solar north-pole polarity, and the bottom of Fig. 12a indicates south-pole polarity. By using the assumption of relativism, the butterfly diagram might be helpful for understanding how the locations of volcanic eruptions periodically vary on Earth—via similar external forcing related to wave mechanics of gaseous SEF-matter.

Also, the strength of each ~10.74-yr sunspot cycle can be measured by the number of sunspots per interval of time (Fig. 12b). When sunspot numbers are large, solar wind blasts tend to be strong, and the latitudes of the sunspots move closer to the poles. For instance, the five strongest solar cycles in Fig. 12b occurred around 1940, 1950, 1960, 1980, and 1990. In all five instances, the "butterfly wings" for those years (Fig. 12a) extended closer toward polar latitudes than for the cycles with weak solar activity. These diagrams of solar latitudes and solar intensities might pertain to volcanic properties for the terrestrial planets. In particular, maxima of the 822-myr UWS cycle might coincide with extremely intense unidirectional compressions of the gaseous SEF-matter. The compressions could be so intense that they exert sufficient pressure from a single direction to push most of the landmass on a tectonic planet toward a pole. This could explain the formation of supercontinents and the associated superchrons that seem to develop simultaneously.

10.4. Theoretical predictions and tests

New theories are generally treated critically, as they should be, until the point when the theory is presented in a falsifiable format, and then the hypothesized cause is described with enough detail to make specific testable predictions. To comply with these theoretical expectations, following are some of the more notable predictions from the Universal Cycle hypothesis—predictions that can be used to test the validity of the hypothesis and model. Some of these predictions already have some observational evidence to support them. In that sense, they might not qualify as true predictions. However, we are unaware of other theories or any researchers making these predictions.

Prediction 1—Episodes of massive volcanic activity have occurred simultaneously on the Moon, Earth, Venus, and Mars. The ages of the greatest volcanic episodes are predicted to coincide with theoretical peaks of the 822-myr

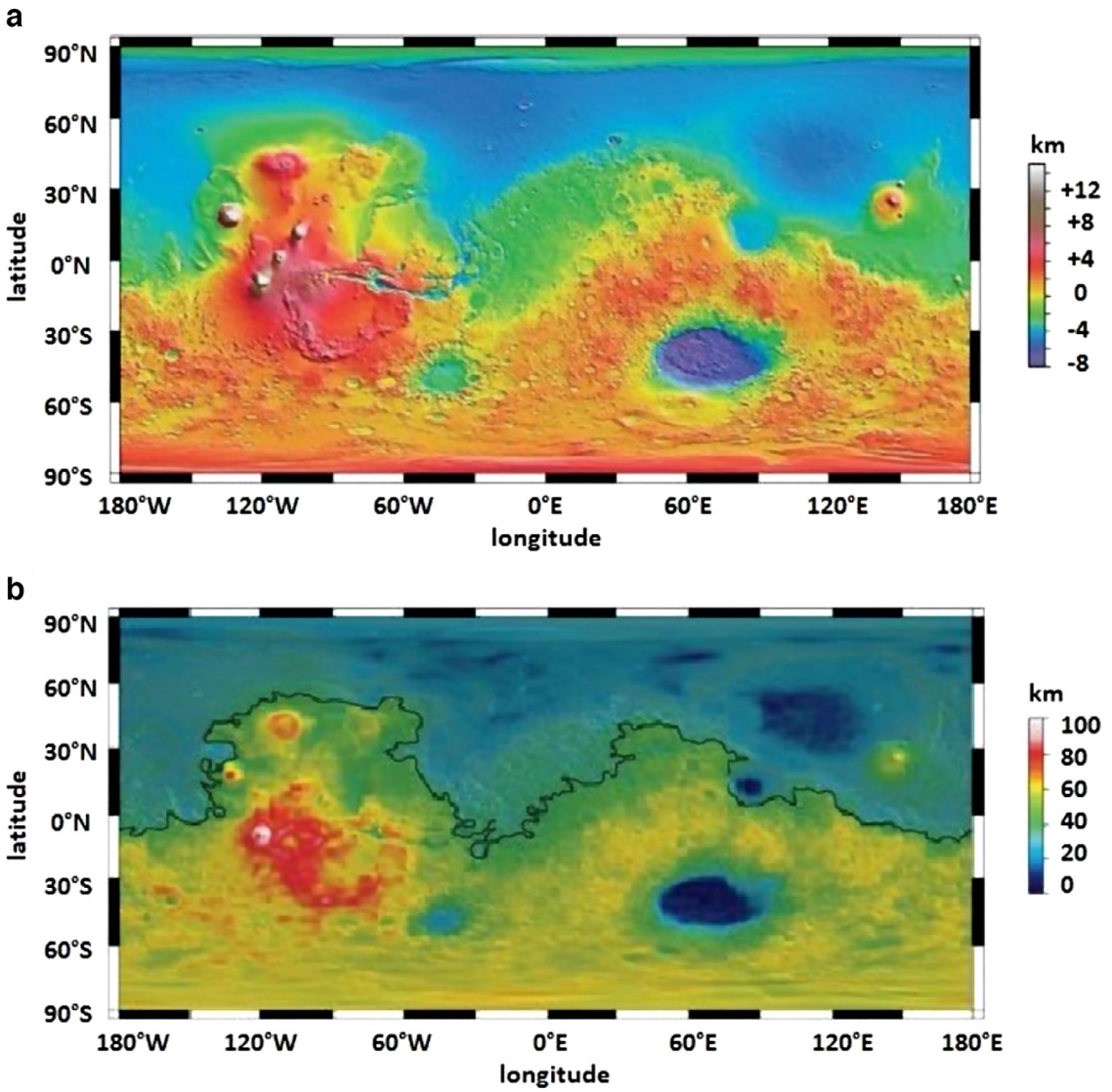

Fig. 13. Two illustrations of the Martian crustal dichotomy, adapted from Watters et al. [107]. (a) Elevation of Martian crust, with blue and green areas designating low-elevation terranes and red and yellow areas designating high-elevation terranes. (b) Thickness of Martian crust, with the black contour line designating regions where the crust is 40 km thick, regions north of the contour have thickness less than 40 km, and regions south of the contour have thickness greater than 40 km. (For interpretation of the references to color in this figure legend, the reader is referred to the web version of this article.)

cycle at 257, 1079, 1901, 2723, 3545, and 4367 Ma. There is already some evidence of this type of synchronous volcanic activity. Specifically, similar clustering of zircons ages from the Moon [35,36], Mars [66], and Earth prompted Neukum et al. [66] to conclude that episodic volcanism follows a common evolutionary track on the Moon and terrestrial planets.

Testing prediction 1—As technologies and space explorations continue to improve, planetary scientists should be able to sample all appropriate surfaces of the terrestrial planets to obtain zircons for age studies. In general, this type of study is already possible for Earth. However, up to this point, all previous attempts to construct a global zircon database over-sampled some continents, under-sampled other continents, and failed to sample other continents. In particular, zircons from Antarctica and Africa were typically grossly under-sampled or completed omitted from the databases. New efforts to evenly sample all continental regions on Earth, by using U-Pb, Lu-Hf, and Sm-Nd dating methods, should provide zircon databases that will show the periodicity of volcanism on Earth with reasonable accuracy. Similar sampling of the Moon is also possible with current technologies, but would obviously be more costly than global sampling of zircons on Earth.

Prediction 2—The Martian crustal dichotomy [67,92,107] results from an unusual distribution of Martian terranes—with almost all southern hemisphere surfaces significantly elevated in comparison to northern hemisphere terranes (Fig. 13a). Furthermore, the crust is significantly thicker in the southern hemisphere than in the northern hemisphere

(Fig. 13b). Watters et al. [107] used subsurface echoing techniques from radar to determine that the crustal dichotomy formed early in the geologic evolution of Mars. The dichotomy could serve as an illustration of how supercontinents appeared on Earth during the early stages of their breakup. Based on the age-distribution of zircons found in meteorites on Earth that were blasted from Mars, in combination with the 822-myr supercontinent cycle, the Universal Cycle hypothesis predicts that the dichotomy formed at ~3545 Ma as a supercontinent at the south pole of Mars. Then, near the trough of the 822-myr cycle (at ~3120 Ma), while the predicted 3545 Ma Martian supercontinent was breaking apart, the dissemination was frozen in time when tectonic activity ceased on Mars.

Testing prediction 2—In addition to zircons blasted from Mars via meteorites, remote sensing techniques continue to improve. The improvements in satellite sensing techniques might reach a point in the next few decades that will permit estimating the age of the southern hemisphere dichotomy with reasonable accuracy. However, a sufficiently large sampling of Martian zircon ages from meteorite sources should give answers about the Martian dichotomy in a timelier manner.

Prediction 3—On the Moon and the terrestrial planets, the locations of the supercontinents are predicted to oscillate between the north and south poles at ~822-myr intervals because of the intense pressure exerted on planetary interiors from the highly compressed and oscillating flows of the gaseous SEF-matter. This prediction is based on the assumption that waves of the gaseous SEF-matter compress and then decompress the same as ordinary mechanical waves. In a compressed phase, the medium (SEF-matter) would be denser than it would be in the subsequent decompressed phase. For example, compressed H_2O molecules exert increased pressure in a sea, which in turn cause the waters to crest as a surface wave at the height of each periodic compression. Similarly, the increased pressure exerted by compressed gaseous SEF-matter would be sufficient to cause baryonic objects, such as Earth's core, to heat and expand. In turn, this would cause the instabilities that contribute to volcanism, solar flares, and star formation. Moreover, the flows and counter-flows associated with mechanical wave compressions and decompressions would provide the mechanism for polarity oscillations—such as geomagnetic reversals. When viewed from the perspective of the extreme volcanic activity and zircon formation associated with the ~822-myr supercontinent cycle, the hypothesis predicts that (a) the locations of major volcanism on the terrestrial planets would coincide with the locations of supercontinents, and (b) the locations would fluctuate synchronously on all of the terrestrial planets from the north poles at ~4367 Ma, to the south poles at ~3545 Ma, back to the north poles at ~2723 Ma, to the south poles at ~1901 Ma, back to the north poles at ~1079 Ma, to the south poles at ~257 Ma, and back to the north poles in another 565-myr.

Testing prediction 3—There is already some limited evidence to support this prediction: (a) the Martian dichotomy appears to have formed around ~3545 Ma at the south-pole because the zircons from meteorites blasted from Mars show that the highest concentration of ages occurs in a range between 3300 Ma and 3900 Ma—with the peak concentration around 3550–3600 Ma, (b) the Pangaea supercontinent formed at the South Pole around 257 Ma, (c) there is some evidence that the Rodinia supercontinent formed at the North Pole around 1079 Ma [61,109]. Improved and concentrated efforts in paleomagnetic research should eventually determine the locations of the supercontinents that developed between the ages of 3000–1000 Ma.

Prediction 4—On Earth, tectonic movements transport zircons from their original formation locations to other regions of the globe. However, tectonic activity has ceased on Mars and the Moon, perhaps around 3120 Ma on both celestial bodies. Thus, zircons that formed after 3120 Ma on Mars and the Moon should be found today in roughly the same locations where they initially formed. Consequently, it is possible to produce a "butterfly diagram" of zircon latitudes versus zircon ages for both of these bodies. Doing so would show if zircons from extraterrestrial plumes produce a diagram similar to the sunspot diagram. The Universal Cycle hypothesis predicts that the terrestrial diagrams would be similar, but perhaps highly skewed (with only one wing) for ages corresponding to supercontinent formation at 822-myr intervals.

Testing prediction 4—When technologies finally permit this type of analysis on the Moon and Mars, the hypothesis predicts that the diagrams will contain an unusually large number of zircons with ages of ~2723 and ~1079 Ma near the north poles, and an unusually large number of zircons with ages of ~1901 and ~257 Ma at the south poles. At a minimum, the hypothesis gives guidance about which regions of the Moon and Mars need to be explored to find rocks (and zircons) of specific ages.

Prediction 5—Three-dimensional mapping of quasar ages might allow researchers to see the curvature of the UWS waves. In turn, the curvature should identify the source of the waves—similar to waves in a pond indicating the source of the motions. This experiment would be challenging, and would require sophisticated computer software because the quasars for any given age are a function of distance from Earth. This produces concentric spheres as snapshots in time—rather than snapshots of all observable regions at the same time. Consequently, any snapshot of quasar ages would only give a small spherical subset of the entire population of quasar formation ages.

Testing prediction 5—Nonetheless, three-dimensional snapshots of a subset of the wave population, overlaid in successions, might help detect the curvatures needed to pinpoint the source of the UWS cycles. If this experimental mapping succeeds, it would allow researchers to "see" regions of the universe far beyond those currently observable via the redshifted light from quasars. Thus, the scientific community would gain a means for measuring astronomical distances well beyond the restrictions imposed by electromagnetic radiation.

11. Conclusions

This research rigorously analyzed the occurrence of quasi-period cycles, referred to as UWS cycles. The cycles are hypothesized to propagate throughout the observable regions of the universe via successive compressions and decompressions of SEF matter. The associated Universal

Cycle hypothesis was used to make five specific predictions, with a brief discussion of how each prediction can be tested. Collectively, the results support the idea of large-scale waves of gaseous-like fractal matter propagating throughout the observed regions of the universe. These cycles primarily occur in a period-tripling sequence of 30.44, 91.33, 274, 822, 2466, and 7398-myr. This hypothesis, best summarized by the Universal Cycle model given in Eq. (3), should be testable beyond all reasonable doubt in coming years as technologies, sampling resolutions, and age-models continue to improve.

Acknowledgements

We thank Andreas Prokoph and Ed Mason for useful feedback from earlier versions of the manuscript.

Supplementary materials

Supplementary material associated with this article can be found, in the online version, at doi:10.1016/j.chaos.2015.09.029.

References

[1] Ackermann M, Asano K, Atwood WB, Axelsson M, Baldini L, Ballet J, et al. Fermi observations of GRB 090510: A short hard gamma-ray burst with an additional, hard power-law component from 10 keV to GeV energies. Astrophys J 2010;716(2):1178–90.
[2] Ahn CP, Alexandroff R, Prieto CA, Anders F, Anderson SF. The tenth data release of the sloan digital sky survey: First spectroscopic data from the SDSS-III apache point observatory galactic evolution experiment. Astrophys J Suppl 2014;211(2):1–16.
[3] Alvarez-Solas J, Charbit S, Ritz C, Paillard D, Ramstein G, Dumas C. Links between ocean temperature and iceberg discharge during Heinrich events. Nat Geosci 2010;3:122–6.
[4] Belozerov VB, Ivanov IA. Platform deposition in the West Siberian plate: A kinematic model. Russian Geol Geophys 2003;44(8):750–61.
[5] Bergemann M, Ruchti GR, Serenelli A, Feltzing S, Alves-Brito A, Asplund M, et al. The Gaia-ESO Survey: radial metallicity gradients and age-metallicity relation of stars in the Milky Way disk. Astron Astrophys 2014;565(A89):1–11.
[6] Berger E, Shin MS, Mulchaey JS, Jeltema TE. Galaxy clusters associated with short GRBs. I. The fields of GRBs 050709, 050724, 050911, and 051221a. Astrophys J 2007;660:496–503.
[7] Biggin AJ, Strik GHMA, Langereis CG. The intensity of the geomagnetic field in the late-Archaean: New measurements and an analysis of the updated IAGA palaeointensity database. Earth Planet Space 2009;61(1):9–22.
[8] Biggin AJ, McCormack A, Roberts A. Palaeointensity database updated and upgraded. EOS Trans Am Geophys Union 2010;91(1):15–16.
[9] Biggin AJ, Steinberger B, Aubert J, Suttie N, Holme R, Torsvik TH, et al. Possible links between long-term geomagnetic variations and whole-mantle convection processes. Nat Geosci 2012;5:526–33.
[10] Biggin AJ, 2014. Absolute Palaeointensity Database (PINT 2014). Unpublished data available at http://earth.liv.ac.uk/pint/
[11] Bloomfield P. Fourier analysis of time series: An introduction. 2nd ed. New York, NY: John Wiley & Sons; 2000.
[12] Butler RF. Paleomagnetism: Magnetic domains to geologic terrains. Boston, MA: Blackwell Scientific Publications; 1992.
[13] Casagrande L, Schoenrich R, Asplund M, Cassisi S, Ramirez I, Melendez J, et al. New constraints on the chemical evolution of the solar neighbourhood and Galactic disc(s). Improved astrophysical parameters for the Geneva-Copenhagen survey. Astron Astrophys 2011;530 A138:1–21.
[14] Chatfield C. The analysis of time series: An introduction. 6th ed. Boca Raton, FL: Chapman & Hall/CRC; 2004.
[15] Coe RS, Glatzmaier GA. Symmetry and stability of the geomagnetic field. Geophys Res Lett 2006;33 L21311:1–5.
[16] Condie KC. What on Earth happened 2.7 billion years ago?. In: EGS-AGU-EUG Joint Assembly, Abstracts from the meeting held in Nice, France; 2003 611 April 2003, abstract #1269.
[17] Condie KC. Preservation and recycling of crust during accretionary and collisional phases of proterozoic orogens: A bumpy road from Nuna to Rodinia. Geosciences 2013;3(2):240–61.
[18] Condie KC, Aster RC. Zircon age episodicity and growth of continental crust. EOS Trans Am Geophys Union 2009;90:364–5.
[19] Condie KC, Davaille A, Aster RC, Arndt N. Upstairs-downstairs: Supercontinents and large igneous provinces, are they related? Intl Geol Rev 2015;57(11–12):1341–8.
[20] Cucchiara A, Fumagalli M, Rafelski M, Kocevski D, Prochaska JX, Cooke RJ, Becker GD. Unveiling the secrets of metallicity and massive star formation using DLAs along gamma-ray bursts. Astrophys J 2015;804(1):1–29.
[21] Dansgaard W, Johnsen SJ, Clausen HB, Dahl-Jensen D, Gundestrup NS, Hammer CU, et al. Evidence for general instability of past climate from a 250-kyr ice-core record. Nature 1993;364:218–20.
[22] Elliott J, Krühler T, Greiner J, Savaglio S, Olivares F, et al. The low-extinction afterglow in the solar-metallicity host galaxy of Gamma-Ray Burst 110918A. Astron Astrophys 2013;556(A23):1–12.
[23] Fan Z, DeGrijs R, Zhow X. An updated catalog of M31 globular-like clusters: UBVRI photometry, ages, and masses. Astrophys J 2010;725(1):200–13.
[24] Fan Z, DeGrijs R. Star clusters in M33: Updated UBVRI photometry, ages, metallicities, and masses. Astrophys J Suppl Ser 2014;211(2) 22:1–13.
[25] Feigenbaum MJ. Universal behavior in nonlinear systems. Phys D: Nonlinear Phenom 1983;7(1–3):16–39.
[26] Fong W, Berger E, Chornock R, Levan AJ, Fruchter AS, Graham JF, et al. The optical afterglow and z = 0.92 early-type host galaxy of the short GRB 100117A. Astrophys J 2011;730 26:1–8.
[27] Forbes DA, Bridges T. Accreted versus in situ Milky Way globular clusters. Mon Not Roy Astron Soc 2010;404:1203–14.
[28] Gradstein FM, Ogg JG, Schmitz MD, Ogg GM. The geologic time scale 2012, two volumes. Boston, MA: Elsevier; 2012.
[29] Greiner, J., 2014. GRBs localized with BSAX, BATSE/RXTE, ASM/RXTE, IPN, HETE, INTEGRAL, Swift, AGILE, Fermi/GLAST, or MAXI. Unpublished data available at http://www.mpe.mpg.de/~jcg/grbgen.html
[30] Guidorzi C, Kobayashi S, Perley DA, Vianello G, Bloom JS, Chandra P, et al. A faint optical flash in dust-obscured GRB 080603A: Implications for GRB prompt emission mechanisms. Mon Not Roy Astron Soc 2011;417(3):2124–43.
[31] Harris J, Zaritsky D. The star formation history of the Large Magellanic Cloud. Astron J 2009;138(5):1243–60.
[32] Hatfield CB, Camp MJ. Mass extinctions correlated with periodic galactic events. Geol Soc Am Bull 1970;81(3):911–14.
[33] Hathaway DH. The solar cycle. Liv Rev Solar Phys 2010;7(1):1–65.
[34] Heinrich H. Origin and consequences of cyclic ice rafting in the Northeast Atlantic Ocean during the past 130,000 years. Quat Res 1988;29(2):142–52.
[35] Hiesinger HJ, Jaumann R, Neukum G, Head JW III. Ages of mare basalts on the lunar nearside. J Geophys Res 2000;105:29239–75.
[36] Hiesinger HJ, Head III JW, Wolf U, Jaumann R, Neukum G. Ages and stratigraphy of mare basalts in Oceanus Procellarum, Mare Nubium, Mare Cognitum, and Mare Insularum. J Geophys Res 2003;108(E7):1–27.
[37] Holmberg J, Nordström B, Andersen J. Geneva-Copenhagen survey of solar neighborhood III. Astron Astrophys 2009;501:941–7.
[38] Hospers J. Rock magnetism and polar wandering. Nature 1954;173:1183–4.
[39] Isley AE, Abbott DH. Implications of the temporal distribution of high-Mg magmas for mantle plume volcanism through time. J. Geol. 2002;110:141–58.
[40] Jacobs JA. The cause of superchrons. Astron Geophys 2001;42(6) 6.306.31.
[41] Jaunsen AO, Rol E, Watson DJ, Malesani D, Fynbo JPU, Milvang-Jensen B, et al. GRB 070306: A Highly extinguished afterglow. Astrophys J 2008;681(1):453–61.
[42] Johnson HP, Van Patten D, Tivey M, Sager WW. Geomagnetic polarity reversal rate for the Phanerozoic. Geophys Res Lett 1995;22(3):231–4.
[43] Joyce M, Labini FS, Gabrielli A, Montouri M, Pietronero L. Basic properties of galaxy clustering in the light of recent results from the Sloan Digital Sky Survey. Asron Astrophys 2005;443(1):11–16.
[44] Kang Y, Rey SC, Bianchi L, Lee K, Kim Y, Sohn ST. A comprehensive GALEX ultraviolet catalog of star clusters in M31 and a study of the young clusters. Astrophys J Suppl 2012;199(2):1–25.
[45] Kashlinsky A, Atrio-Barandela F, Kocevski D, Ebeling H. A measurement of large-scale peculiar velocities of clusters of galaxies: Results and cosmological implications. Astrophys J 2008;686(2):L49–52.
[46] Kashlinsky A, Atrio-Barandela F, Ebeling H, Edge A, Kocevski D. A new measurement of the bulk flow of x-ray luminous clusters of galaxies. Astrophys J Lett 2010;712(1):L81–5.

[47] Kessler R, Becker AC, Cinabro D, Vanderplas J, Frieman JA, Marriner J, et al. First-year Sloan Digital Sky Survey-II supernova results: Hubble diagram and cosmological parameters. Astrophys J Suppl 2009;185(1):32–84.
[48] Komatsu E, Smith KM, Dunkley J, Bennett CL, Gold B, Hinshaw G, et al. Seven-year Wilkinson Microwave Anisotropy Probe (WMAP) observations: Cosmological interpretation. Astrophys J Suppl 2011;192(2) 18:1–47.
[49] Korenaga J. Archean geodynamics and the thermal evolution of earth. Archean geodynamics and environments. Benn K, Mareschal JC, Condie KC, editors. Washington, DC: American Geophysical Union; 2006.
[50] Krühler T, Malesani D, Milvang-Jensen B, Fynbo JPU, Hjorth J, Jakobsson P, et al. The optically unbiased GRB host (TOUGH) survey. V. VLT/X-shooter emission-line redshifts for Swift GRBs at z ∼2. Astrophys J 2012;758(1) 46:1–8.
[51] Laskar T, Berger E, Tanvir N, Zauderer BA, Margutti R, Levan A, et al. GRB 120521C at z ∼6 and the properties of high-redshift GRBs. Astrophys J 2013;781(1):1–24.
[52] Longo MJ. Detection of a dipole in the handedness of spiral galaxies with redshifts z ∼0.04. Phys Lett B 2011;699(4):224–9.
[53] Loper DE, McCartney K, Buzyna G. A model of correlated episodicity in magnetic-field reversals, climate, and mass extinctions. J Geol 1988;96:1–15.
[54] Lourens LJ, Becker J, Bintanja R, Hilgen FJ, Tuenter E, van deWal RSW, et al. Linear and non-linear response of late Neogene glacial cycles to obliquity forcing and implications for the Milankovitch theory. Quat Sci Rev 2010;29:352–65.
[55] Lutz TM. The magnetic reversal record is not periodic. Nature 1985;317:404–7.
[56] Mandelbrot B. How long is the coast of britain? statistical self-similarity and fractional dimension.. Science 1967;156(3775):636–8.
[57] Mazaud A, Laj C, de Sèze L, Versoub KL. 15-Myr periodicity in the frequency of geomagnetic reversals since 100 Ma. Nature 1983;304:328–30.
[58] McCaffrey KJW, Petford N. Are granitic intrusions scale invariant? J Geol Soc 1997;154:1–4.
[59] McCulloch MT, Bennett VC. Progressive growth of the Earth's continental crust and depleted mantle geochemical constraints. Geochim Cosmochim Acta 1994;58:4717–38.
[60] McElhinny M.W., 2007. Geocentric axial dipole hypothesis, in Encyclopedia of Geomagnetism and Paleomagnetism. In Gubbins, D., and E. Herrero-Bervera, editors. Dordrecht: Springer, pp. 281–286.
[61] Meert JG, Torsvik TH. The making and unmaking of a supercontinent: Rodinia revisited. Tectonophysics 2003;375(1–4):261–88.
[62] NASA, 2014. GCN circulars archive. Unpublished data available at http://gcn.gsfc.nasa.gov/gcn3_archive.html
[63] Negi JG, Tiwari RK. Matching long term periodicities of geomagnetic reversals and galactic motions of the solar system. Geophys Res Lett 1983;10(8):713–16.
[64] Negi JG, Tiwari RK, Rao KNN. Clean spectral analysis of long-term sea-level changes. Terra Nova 1990;2(2):138–41.
[65] Negi JG, Tiwari RK, Rao KNN. Clean periodicity in secular variations of dolomite abundance in deep marine sediments. Marine Geol 1996;133(1–2):113–21.
[66] Neukum G, Basilevsky AT, Kneissl T, Chapman MG, vanGasselt S, et al. The geologic evolution of Mars: Episodicity of resurfacing events and ages from cratering analysis of image data and correlation with radiometric ages of Martian meteorites. Earth Planet Sci Lett 2010;294(3–4):204–22.
[67] Neumann GA, Zuber MT, Wieczorek MA, McGovern PJ, Lemoine FG, Smith DE. The crustal structure of Mars from gravity and topography. J Geophys Res 2004;109 E08002:1–18.
[68] Oates SR, Page MJ, Schady P, De Pasquale M, Evans PA, Page KL, et al. A statistical comparison of the optical/UV and X-ray afterglows of gamma-ray bursts using the Swift Ultraviolet Optical and X-ray Telescopes. Mon Not Roy Astron Soc 2011;412:561–79.
[69] Pechersky DM. Neogea paleomagnetism constraints on the processes in the core and at the surface of the Earth. Russian J Earth Sci 1998;1(2):103–35.
[70] Pechersky DM, Lyubushin AA, Sharonova ZV. On the coherence between changes in biota and geomagnetic reversals in the Phanerozoic. Izvest Phys Solid Earth 2012;48(1):42–60.
[71] Pelletier J. Coherence resonance and ice ages. J Geophys Res 2003;108(D20) 4645:1–14.
[72] Perley DA, Li W, Chornock R, Prochaska JX, Butler NR, Chandra P, et al. GRB 071003: Broadband follow-up observations of a very bright gamma-ray burst in a galactic halo. Astrophys J 2008;688:470–90.
[73] Perley DA, Bloom JS, Klein CR, Covino S, Minezaki T, Woźniak P, et al. Evidence for supernova-synthesized dust from the rising afterglow of GRB 071025 at z ∼5. Mon Not Roy Astron Soc 2010;406(4):2473–87.
[74] Perley DA, Perley RA. Radio constraints on heavily obscured star formation within dark gamma-ray burst host galaxies. Astrophys J 2013;778(2) 172:1–10.
[75] Perrin M, Schnepp E. IAGA paleointensity database: Distribution and quality of the data set. Phys Earth Planet Interior 2004;147:255–67.
[76] Phillips JD, Cox A. Spectral analysis of geomagnetic reversal time scales. Geophys J Inter 1976;45(1):19–33.
[77] Pietronero L. The fractal structure of the universe: Correlations of galaxies and clusters and the average mass density. Phys A 1987;144(2–3):257–84.
[78] Pisarevsky S. New edition of the global paleomagnetic database. EOS Trans Am Geophys Union 2005;86(17):170.
[79] Prokoph A, Puetz SJ. Period-tripling and fractal features in multi-billion year geological records. Math Geosci 2015;47(5):501–20.
[80] Puetz SJ, Prokoph A, Borchardt G, Mason E. Evidence of synchronous, decadal to billion year cycles in geological, genetic, and astronomical events. Chaos Soliton Fractal 2014;62-63:55–75.
[81] Rampino MR, Stothers RB. Terrestrial mass extinctions, cometary impacts and the Sun's motion perpendicular to the galactic plane. Nature 1984;308:709–12.
[82] Rampino MR, Stothers RB. Flood basalt volcanism during the past 250 million years. Science 1988;241(4866):663–8.
[83] Raup DM, Sepkoski JJ. Mass extinctions in the marine fossil record. Science 1982;215:1501–3.
[84] Raup DM. Magnetic reversals and mass extinctions. Nature 1985;314:341–3.
[85] Rowlinson A, Wiersema K, Levan AJ, Tanvir NR, O'Brien PT, Rol E, et al. Discovery of the afterglow and host galaxy of the low redshift short GRB 080905A. Mon Not Roy Astron Soc 2010;408:383–91.
[86] Scafetta N, Willson RC. Planetary harmonics in the historical Hungarian aurora record (1523–1960). Planet Space Sci 2013;78:38–44.
[87] Scargle JD. Studies in astronomical time series analysis. II—Statistical aspects of spectral analysis of unevenly spaced data. Astrophys J 1982;263:835–53.
[88] Schneider DP, Richards GT, Hall PB, Strauss MA, Anderson SF, Boroson TA, et al. The sloan digital sky survey quasar catalog. V. Seventh data release. Astron J 2010;139(6):2360–73.
[89] Schulz M, Mudelsee M. REDFIT: Estimating red-noise spectra directly from unevenly spaced paleoclimatic time series. Comput Geosci 2002;28:421–6.
[90] Schulze S, Malesani D, Cucchiara A, Tanvir NR, Krühler T, de Ugarte-Postigo A, et al. GRB 120422A/SN 2012bz: Bridging the gap between low- and high-luminosity gamma-ray bursts. Astron Astrophys 2014;566(A102):1–31.
[91] Shen SZ, Crowley JL, Wang Y, Bowring SA, Erwin DH, et al. Calibrating the end-permian mass extinction. Science 2011;334(6061):1367–72.
[92] Smith DE, Zuber MT, Frey HV, Garvin JB, Head JW, et al. Mars orbiter laser altimeter: Experiment summary after the first year of global mapping of Mars. J Geophys Res 2001;106(E10):23689–722.
[93] Starling RLC, Wiersema K, Levan AJ, Sakamoto T, Bersier D, Goldoni P, et al. Discovery of the nearby long, soft GRB 100316D with an associated supernova. Mon Not Roy Astron Soc 2010;411(4):2792–803.
[94] Stoica P, Moses R. Spectral analysis of signals. Upper Saddle River, NJ: Prentice-Hall; 2005.
[95] Stothers RB. Periodicity of the Earth's magnetic reversals. Nature 1986;332:444–6.
[96] Tauxe L, Yamazaki T. Paleointensities, in treatise on geophysics. In: Schubert G, editor. Geomagnetism, vol. 5. Oxford: Elsevier; 2007. p. 509–64.
[97] Tiwari RK, Rao KNN. Correlated variations and periodicity of global CO2, biological mass extinctions, and extra-terrestrial bolide impacts over the past 250 million years, and possible geodynamical implications. Geofizika 1998;15:103–16.
[98] Tiwari RK, Rao KNN. Periodicity in marine phosphorus burial rate. Nature 1999;400:31–2.
[99] Tiwari RK, Rao KNN. A statistically significant long-term characteristic time scale of test size variation of calcareous trochospiral benthic foraminifera (CTBF) during the past 120 myr. Geophys Res Lett 2003;30(5):211–14.
[100] Tome AR, Miranda PMA. Continuous partial trends and low-frequency oscillations of time series. Nonlinear Process Geophys 2005;12:451–60.
[101] Turcotte DL. Fractals and fragmentation. J Geophys Res 1986;91(B2):1921–6.

[102] Uffen RJ. Influence of the Earth's core on the origin and evolution of life. Nature 1963;198(4876):143–4.
[103] Veikkolainen T, Pesonen LJ, Evans DAD. PALEOMAGIA, a PHP/MYSQL paleomagnetic database for the Precambrian. Stud Geophys Geod 2014;58(3):425–41.
[104] Veikkolainen T, Evans DAD, Korhonen K, Pesonen LJ. On the low-inclination bias of the Precambrian geomagnetic field. Precamb Res 2014;244:23–32.
[105] Veikkolainen T, Pesonen L, Korhonen K. An analysis of geomagnetic field reversals supports the validity of the Geocentric Axial Dipole (GAD) hypothesis in the Precambrian. Precamb Res 2014;244:33–41.
[106] Voice PJ, Kowalewski M, Eriksson KA. Quantifying the timing and rate of crustal evolution: global compilation of radiometrically dated detrital zircon grains. J Geol 2011;119:109–26.
[107] Watters TR, McGovern PJ, Irwin III RP. Hemispheres apart: The crustal dichotomy on Mars. Ann Rev Earth Planet Sci 2007;35:621–52.
[108] Wendler J. External forcing of the geomagnetic field? Implications for the cosmic ray flux—Climate variability. J Atmos Solar-Terr Phys 2004;66:1195–203.
[109] Zhao G, Cawood PA, Wilde SA, Sun M. Review of global 2.1–1.8 Ga orogens: Implications for a pre-Rodinia supercontinent. Earth-Sci Rev 2002;59(1–4):125–62.